学位論文

Ultrafast hydrogen migration in methanol by pump-probe coincidence momentum imaging method with few-cycle laser pulses

(数サイクルレーザーパルスを用いたポンプ-プローブコインシデンス運動量画像法によるメタノール分子の超高速水素マイグレーション)

平成 26 年 12 月博士 (理学) 申請

東京大学大学院理学系研究科

化学専攻

安藤　俊明

Abstract

Ultrafast hydrogen migration and fragmentation dynamics in methanol induced by few-cycle intense laser pulses was investigated by using pump-probe coincidence momentum imaging (CMI) method. In chapter 1, interaction between molecules and intense laser field is introduced as a general introduction.

In chapter 2 and 3, the experimental setup for this study is introduced including the generation and characterization of the few-cycle laser pulses, the ultra-high vacuum chamber for pump-probe coincidence momentum imaging measurement and data analysis methods. The few-cycle pulses, of which spectral phase is well-flattened, were generated by constructing the feedback system to compensate the spectral phase of the fundamental pulses. In the pump-probe coincidence measurement, the time delay between pump and probe pulses was smoothly scanned to average out the fluctuation of experimental conditions. The momentum of fragment ions and the time delay were recorded and the delay dependent momentum images of fragment ions were constructed after the measurement. The fragment ion pares decomposed through Coulomb explosion pathways were extracted from the data set by applying coincidence momentum imaging method. The number of false coincidence events was estimated by expanding the definition of the covariance mapping method.

In chapter 4, ultrafast hydrogen migration in methanol observed by pump-probe coincidence momentum imaging is discussed. In the non-migration pathway, C-O bond breaking of CH_3OH^+ was observed in real time. In migration pathway, the vibrational motions along the C-O bond of $CH_2OH_2^+$

were observed. It is concluded that the ultrafast hydrogen migration occurs $\sim$25 fs after internal conversion.

H_3^+ emission from methanol dication is discussed in chapter 5. It is considered that H_3^+ emission pathway is predissociation process from long lived dication. The ion yield of H_3^+ was periodically changed in the time delay. This period can be assigned to the C-O stretching vibration of cation. It is considered that the vibrational energy of dication is changed in time delay and the rate of H_3^+ emission is changed. This study is summarized in chapter 6 and future perspective is proposed.

Contents

1 Introduction

Development of laser technology helps us to understand interactions between molecules and light. Ultra-short laser pulses can be utilized to observe the molecular dynamics in real-time. After the invention of the laser, the pulsed laser has been developed. Nowadays, the pulse duration is close to the optical cycle in wavelength range from visible to near infra-red. We can observe the vibrational motion of molecules with this pulse. In EUV region, the pulse duration reach down to attosecond regime. The motions of electrons in valence bands can be observed with the attosecond pulses [1].

Improvement of peak intensity of the laser pulses enable us to investigate interaction between the molecules and intense laser fields, whose strength is comparable to the Coulomb fields generated by an atomic nucleus [2]. The molecules exposed by the intense laser fields are ionized via tunnelling effect, the nuclear motion can be regard as the time evolution of the vibrational wave packet on the light-dressed potential energy surfaces.
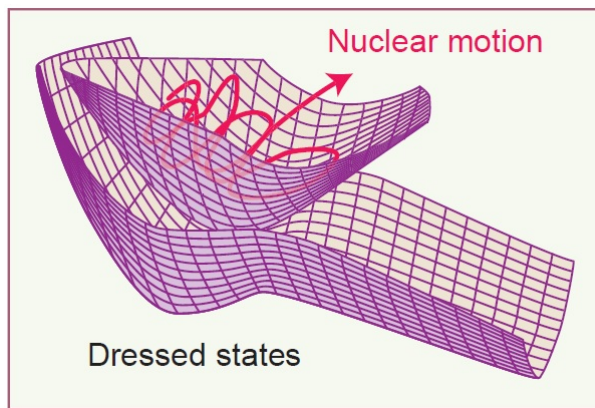

Figure 1.1: Schematics of nuclear motion on the light dressed potential energy surfaces shown in Ref. [2].

When hydrocarbon molecules are exposed by the intense laser field, those geometrical structure changes with the motion of hydrogen atoms within tens of femtosecond, which is called ultrafast hydrogen migration. In 2004, the ultrafast hydrogen migration in acetonitrile induced by the intense femtosecond laser field were observed with coincidence momentum imaging (CMI) method [3], that is,

$$CH_3CN^{2+} \rightarrow CH_{3-n}^+ + H_nCN^+ \ (n = 0, 1, 2).$$

It was considered that the hydrogen atoms in the methyl group migrate and Coulomb explosion take place just after the double ionization. It was concluded that the hydrogen migration proceeds in tens of femtosecond time scale. After the first observation of the hydrogen migration, the hydrogen migration has been observed in many hydrocarbon species [4–7]. It was considered that the hydrogen migration progressed with following process. The hydrocarbon molecules ionized to the cation by the laser field and one of the hydrogen atoms migrates. After that, the cation is ionized to doubly charged manifold and decomposed via Coulomb explosion process immediate.

In 2007, hydrogen migration in acetylene induced by sub-10 fs laser pulse was traced with pump-probe CMI method in real-time [8]. Three-body Coulomb explosion pathway,

$$C_2D_2^{3+} \rightarrow D^+ + C^+ + CD^+,$$
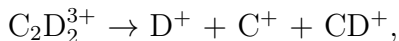
was extracted and the ejected angle of D^+ respect to the C-C bond as a function of the pump-probe time delay. It was revealed that the hydrogen atom in doubly charged acetylene migrates to the other cite. The hydrogen motion was interpreted as a motion of the vibrational wave packet on the potential energy surface of the
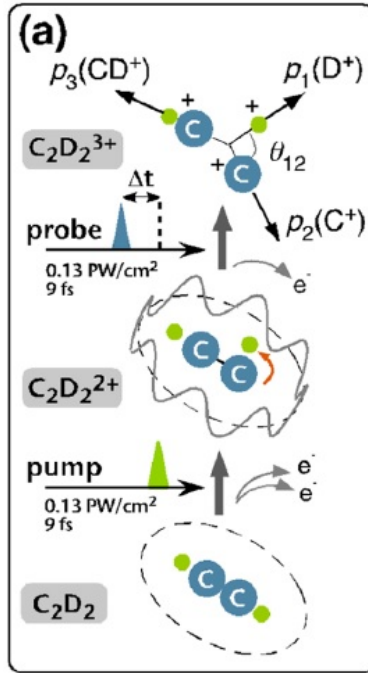
Figure 1.2: Pump-probe Coulomb explosion imaging employed in Ref. [8].

electronically ground state. One of the hydrogen atoms migrates to the other carbon cite at around 90 fs and moves back to the original carbon cite at around 280 fs. Acetylene dication is so stable that it can be detected by time of flight. This is one of the reason that hydrogen migration takes place in doubly charged manihold.

In 2010, it was confirmed that the hydrogen migration in methanol takes place in singly charged manifold by pump-probe CMI with 38 fs laser pulses [9]. In this experiment, the shortest time delay was set to 100 fs to avoid the optical interference of pump and probe laser pulses. The hydrogen migration completes within tens of femtosecond.

In this study, I investigated the hydrogen migration in methanol cation. I performed the pump-probe CMI with few-cycle laser pulses to investigate the hydrogen migration in methanol. If the hydrogen migration proceeds in the absence of the
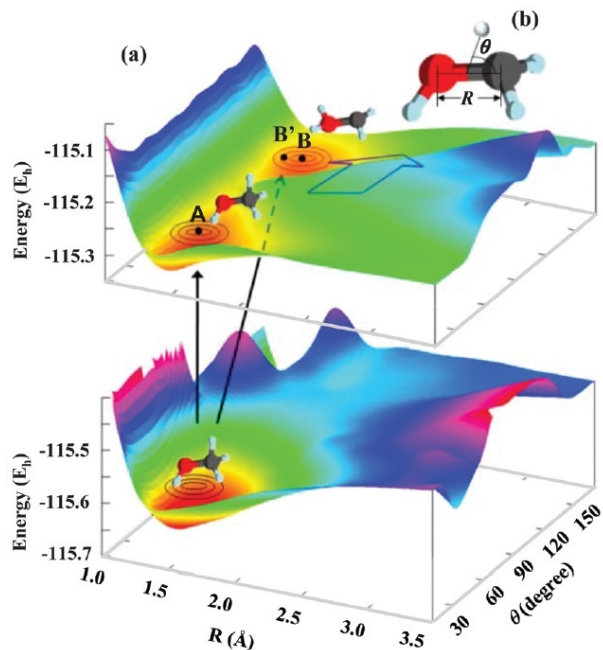
Figure 1.3: $CH_2OH_2^+$ is created within the laser pulse shown in Ref. [9].

laser field, the motion of hydrogen can be considered as the motion of vibrational wave packet on the potential energy surfaces including nonadiavatic transition and the electronic states can be assigned. The determination of the potential energy surfaces contributing to the hydrogen migration is the first step to design the femtosecond laser field in order to control the hydrogen migration.

In chapter 2, the generation of few-cycle pulses is introduced. The experimental setup prepared for the pump-probe CMI method is introduced in chap. 3. In chapter 4, hydrogen migration in methanol are introduced. In hydrogen migration pathway, the vibrational motion along the C-O bond is observed and the wave packet bifurcates into dissociative and bound component in $CH_2OH_2^+$ structure.

In chapter 5, the pump-probe time delay dependence on ion yield of fragment ions is investigated in methanol molecule. By irradiating the few-cycle laser pulse to
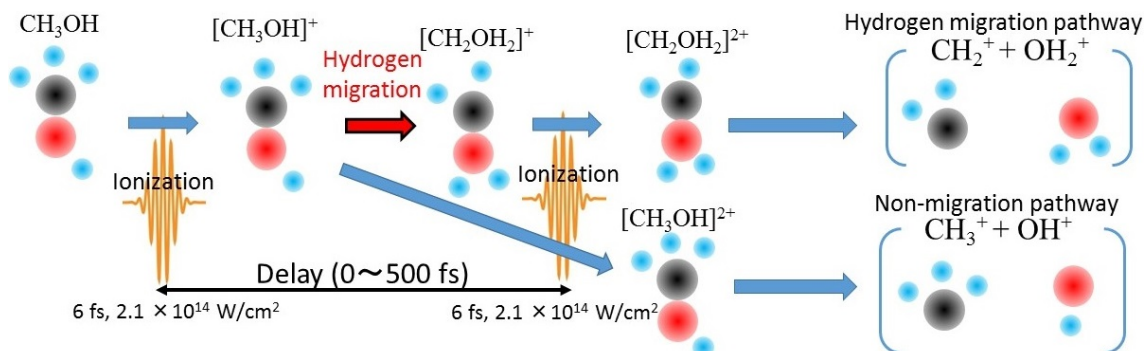
Figure 1.4: Schematics of pump-probe coincidence momentum imaging of methanol performed in this study.

methanol molecule, the vibrational wave packet is prepared. The vibrational wave packet moves along all the vibrational mode. By extracting oscillatory change of ion yield and assign the vibrational mode, the reactivity dependence on the geometrical structure of the molecule can be investigated. This type of experiment is performed by preparing rotational wave packet. The rotational wave packet is prepared by nonadiabatic alignment method and angular dependence of ionization probability is observed. In this study, periodical ion yield are observed in H^+ and H_3^+ emission Coulomb explosion pathway, CH_3OH^+ and CH_3O^+ with same period. This period is assigned to the C-O bond stretching vibration of CH_3OH^+.

In chapter 6, this work is summarized and future perspective is proposed.

References

[1] F. Krausz and M. Ivanov. Attosecond physics. *Reviews of Modern Physics*, 81:163–234, 2009.

[2] K. Yamanouchi. The next frontier. *Science*, 295:1659–1660, 2002.

[3] A. Hishikawa, H. Hasegawa, and K. Yamanouchi. Hydrogen migration in acetonitrile in intense laser fields in competition with two-body Coulomb explosion. *Journal of Electron Spectroscopy and Related Phenomena*, 141:195–200, 2004.

[4] T. Okino, Y. Furukawa, P. Liu, T. Ichikawa, R. Itakura, K. Hoshina, K. Yamanouchi, and H. Nakano. Coincidence momentum imaging of ultrafast hydrogen migration in methanol and its isotopomers in intense laser fields. *Chemical physics letters*, 423:220–224, 2006.

[5] H. Xu, T. Okino, and K. Yamanouchi. Tracing ultrafast hydrogen migration in allene in intense laser fields by triple-ion coincidence momentum imaging. *The Journal of Chemical Physics*, 131, 2009.

[6] H. Xu, T. Okino, K. Nakai, K. Yamanouchi, S. Roither, X. Xie, D. Kartashov, M. Schöffler, A. Baltuška, and M. Kitzler. Hydrogen migration and C-C bond breaking in 1, 3-butadiene in intense laser fields studied by coincidence momentum imaging. *Chemical Physics Letters*, 484:119–123, 2010.

[7] T. Okino, A. Watanabe, H. Xu, and K. Yamanouchi. Two-body Coulomb explosion in methylacetylene in intense laser fields: double proton migration and

proton/deuteron exchange. *Physical Chemistry Chemical Physics*, 14:4230–4235, 2012.

[8] A. Hishikawa, A. Matsuda, M. Fushitani, and E. J. Takahashi. Visualizing recurrently migrating hydrogen in acetylene dication by intense ultrashort laser pulses. *Physical Review Letters*, 99:258302, 2007.

[9] H. Xu, C. Marceau, K. Nakai, T. Okino, S. L. Chin, and K. Yamanouchi. Communication: Two stages of ultrafast hydrogen migration in methanol driven by intense laser fields. *The Journal of Chemical Physics*, 133, 2010.

2 Generation and characterization of few-cycle pulses

2.1 Introduction

In order to obverse the molecular dynamics in real-time, sub-10 femtosecond laser pulses are useful since the typical vibration period of molecules is several tens of femtosecond or longer. These laser pulses are called few-cycle pulses if the wavelength is visible to near-infra-red region. Thanks to the development of laser technology, we can easily generate the few-cycle laser pulses from Kerr lens mode-locked Ti:sapphire oscillator in nano-joule level [1]. However, when these pulses are amplified to millijoule level with conventional chirped-pulse amplification (CPA) method, spectral narrowing takes place and the pulse duration of amplified laser pulses is stretched to longer than 20 fs. To generate few-cycle pulses in millijoule level, several method is proposed and realized. There are two types of the basic idea. The first idea is avoiding band-narrowing. The second idea is obtaining coherent broadband spectrum from the output of CPA laser system.

In this work, few-cycle pulses were generated from the CPA laser system by using hollow-core fiber compression method and characterized with two-dimensional spectral interferometer (2DSI). The obtained result of temporal electric waveform of few-cycle laser pulses was compared with the result of fringe resolved second-order autocorrelator (FRAC).

To generate the few-cycle pulse which has significantly small pedestal structure, alignment of the CPA laser system is also important. If the output of the CPA laser system has pedestal structure in time, the shape of the output spectrum and spectral

phase of the hollow-core fiber becomes complex. After the hollow-core fiber, spectral phase was compensated by using negative chirped mirrors, which is well-designed for compensating positive chirp caused by air and fused silica. The residual spectral phase was finely minimized by changing the propagating thickness of wedge plates made of fused silica. There is only one degree of freedom to compensate the spectral phase continuously. The complex spectral phase structure cannot be removed by this method.

For this reason, the spectral phase of output of the CPA laser system was measured by 2DSI and compensated with an acousto-optic programmable dispersive filter (DAZZLER, FASTLITE) installed between stretcher and regenerative amplifier in the CPA laser system. The pulse duration of the CPA laser system was closed to the Fourier-transform limit of the spectrum. After the fiber and chirped mirrors, the pulse duration was measured to be 6 fs by the 2DSI and the FRAC.

2.2   Spectral phase optimization of fundamental pulse with DAZZLER and 2DSI

2DSI is one of the spectral shearing method invented in 2006 to measure the spectral phase of femtosecond laser pulse [2]. Figure 2.1 shows optical layout of the 2DSI constructed for this study. The input pulse is separated by the surface of the 100 mm SF10 rod, which acts as a dispersive medium. After propagating in the SF10 rod, the pulse duration is stretched to several picoseconds. This stretched pulse is introduced into the interferometer to make replica pulse with certain temporal
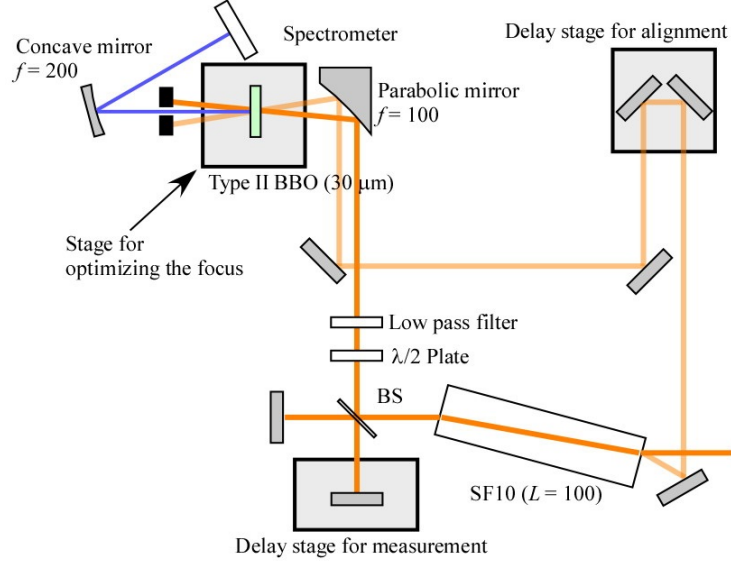
Figure 2.1: Schematics of 2DSI.

delay. The reflation of SF10 and two stretched pulses are focused to the type-II β-barium borate (BBO) crystal, which generates two upconverted pulses of the reflected pulse with different center frequency, in non-collinear orientation. The upconverted pulses propagate to different direction from the reflected pulse and stretched pulses. The upconverted pulses are introduced into the spectrometer. From the spectral interference between the two upconverted pulses, the spectral phase of the reflected pulse can be obtained.

$$E(t) = \frac{1}{2\pi} \int \tilde{E}(\omega) e^{i\omega t} d\omega \qquad (2.1)$$

$$\tilde{E}(\omega) = \int E(t) e^{-i\omega t} dt \qquad (2.2)$$

$$\tilde{E}(\omega) = \sqrt{I(\omega)} e^{i\theta(\omega)} \qquad (2.3)$$

Equations 2.1, 2.2 and 2.3 show the relationship between the temporal shape of the electric fields $E(t)$ and the spectrum $I(\omega)$. The time evolution of the electric fields of femtosecond laser pulses can be constructed by the inverse Fourier transform of the frequency component as shown in Eq. 2.1. The signal intensity obtained with spectrometer is square of $|\tilde{E}(\omega)|$. The remaining problem to obtain the temporal shape of electric field is how to measure the spectral phase $\theta(\omega)$. The Fourier transform of the electric field is shown in Eq. 2.2.

The principle of 2DSI can be described as follows. The generation of upconverted pulse in the BBO crystal is second-order nonlinear optical phenomena. The stretched pulses are quasi-CW pulses for the reflected pulse because the carrier frequency of stretched pulses is monotonically changed in time but the change is significantly slow compared with the pulse duration of the reflected pulse. The center frequency of two quasi-CW pulses can be controlled by the delay between the reflected pulse and the stretched pulses. Second-order nonlinear process between the reflected femtosecond laser pulse $E(t)$ and one of the two quasi-CW laser pulses $E_1 \cos(\omega_1(t - \tau) + \theta_1)$, whose delay τ can be scanned, can be written as Eq. 2.4. The first term corresponds to upconverted component and the second term is differential frequency generation (DFG). The nonlinear process between $E(t)$ and the other quasi-CW laser pulse $E_2 \cos((\omega_1 + \Omega)t + \theta_2)$, whose delay is fixed but the frequency is separated by Ω, is

written in eq. 2.5.

$$
\begin{aligned}
E_{2\text{scan}}(\omega) &= \int E(t)E_1\cos(\omega_1(t-\tau)+\theta_1)e^{-i\omega t}dt \\
&= \frac{1}{2}\tilde{E}(\omega-\omega_1)e^{i(-\omega_1\tau+\theta_1)} + \frac{1}{2}\tilde{E}(\omega+\omega_1)e^{-i(-\omega_1\tau+\theta_1)} \quad (2.4) \\
E_{2\text{fix}}(\omega) &= \int E(t)E_2\cos((\omega_1+\Omega)t+\theta_2)e^{-i\omega t}dt \\
&= \frac{1}{2}\tilde{E}(\omega-\omega_1-\Omega)e^{i\theta_2} + \frac{1}{2}\tilde{E}(\omega+\omega_1)e^{-i(-\omega_1\tau+\theta_1)} \quad (2.5)
\end{aligned}
$$

By introducing the two upconverted pulses into the spectrometer, the interference between these pulses are observed, which include the information of spectral phase as shown in eq. 2.6. The interference pattern depends on the τ.

$$
\begin{aligned}
I(\omega,\tau) &= |\tilde{E}(\omega-\omega_1)e^{i(-\omega_1\tau+\theta_1)} + \tilde{E}(\omega-\omega_1-\Omega)e^{i\theta_2}|^2 \\
&= |\tilde{E}(\omega-\omega_1)e^{i(-\omega_1\tau+\theta_1)}|^2 + |\tilde{E}(\omega-\omega_1-\Omega)e^{i\theta_2}|^2 \\
&\quad +2|\tilde{E}(\omega-\omega_1)\tilde{E}(\omega-\omega_1-\Omega)| \\
&\quad \cos(\theta(\omega-\omega_1)-\theta(\omega-\omega_1-\Omega)-\omega_1\tau+\theta_1-\theta_2) \quad (2.6)
\end{aligned}
$$

The relationship between the $\tau(\omega)$, which have the strongest signal in ω, and the group delay of measured pulse $\frac{d\theta(\omega-\omega_1)}{d\omega} = \tau_g(\omega-\omega_1)$ is

$$
\theta(\omega-\omega_1)-\theta(\omega-\omega_1-\Omega) \simeq \tau_g(\omega-\omega_1)\Omega \quad (2.7)
$$

$$
\theta(\omega-\omega_1)-\theta(\omega-\omega_1-\Omega)-\omega_1\tau(\omega)+\theta_1-\theta_2 = 0 \quad (2.8)
$$

$$
\tau_g(\omega-\omega_1) \simeq \frac{1}{\Omega}(\omega_1\tau(\omega)-\theta_1+\theta_2). \quad (2.9)
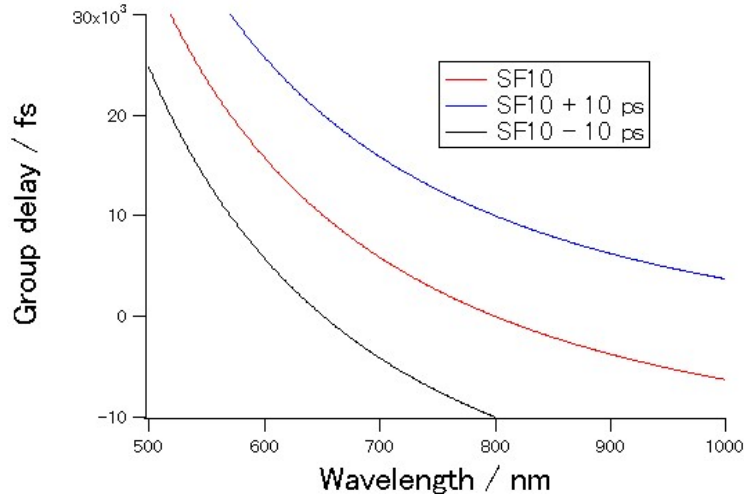$$

Figure 2.2: Group delay of a 100 mm SF10 as a function of wavelength.

In the measurement, the signal intensity along τ is fitted with cosine curve to obtain the $\tau(\omega)$ and ω_1. The calibration of Ω is discussed later. The τ_g is integrated along ω to obtain $\theta(\omega - \omega_1)$.

$$\theta(\omega - \omega_1) = \int \tau_g(\omega - \omega_1)d\omega \tag{2.10}$$

$$\simeq \int \frac{1}{\Omega}(\omega_1\tau(\omega) - \theta_1 + \theta_2)d\omega \tag{2.11}$$

A constant of integration and "$-\theta_1 + \theta_2$", which contribute to the carrier-envelope phase and the group delay, respectively, can not be determined but the envelope of the pulse is independent of these values.

Figure 2.2 shows group delay of a 100 mm SF10 rod, which is the main dispersive medium used in the 2DSI. The Ω and the ω_1 are set to around $2\pi\cdot$ 2 THz ($\Delta\lambda \simeq 4$ nm) and $2\pi\cdot$ 375 THz (800 nm), respectively, in the measurement of out put of the CPA laser system. The corresponding delay is around 200 fs, which is much smaller
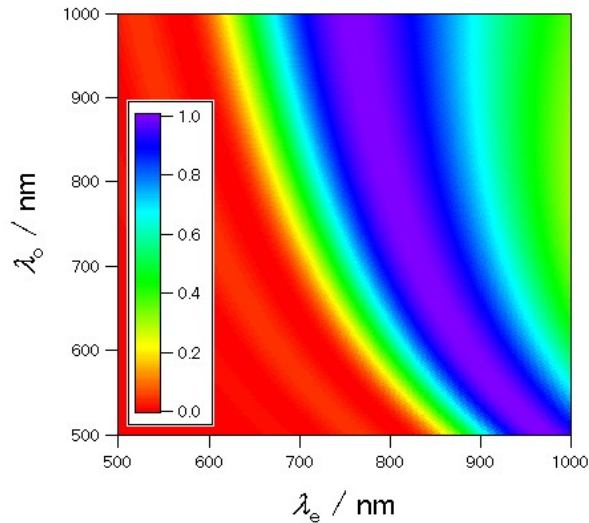
Figure 2.3: Conversion efficiency of the BBO crystal.

than the pulse duration ($\sim$30 fs) and scan range ($\sim$10 fs). This means that the ω_1 and Ω can be considered as a constant. After the interferometer, low-pass filter is inserted to avoid to generate upconverted pulses with other quasi-CW components. The reflection from back surface of the 1 mm thickness beam splitter is also focused with 10 ps time delay if the filter is not inserted.

Figure 2.3 shows conversion efficiency of the BBO crystal (typeII, thickness: 30 μm, crystal angle: 42°). The polarization directions of the stretched pulses are rotated by the half-wave plate and set to parallel with the extraordinary axis to satisfy the phase matching condition in broadband wavelength region for the measured pulse. The ω_1 is set to lower frequency than the center frequency of few-cycle pulse. Figure 2.4 shows result of feedback system. The spectral phase of fundamental pulses was measured by 2DSI and the spectral phase was compensated by DAZZLER. The filled red curve shows spectrum of upconverted pulse. The ω_1 was calibrated by comparing the center frequency of fundamental pulse and upconverted
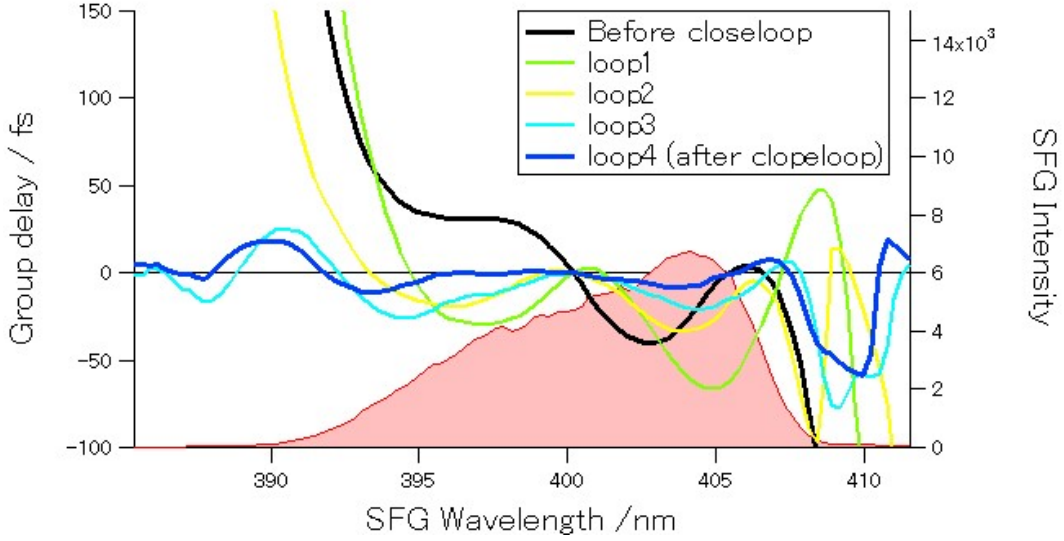
Figure 2.4: Result of feedback loop composed of the 2DSI and the DAZZLER.

pulse and the Ω was also determined from the center frequencies of the two upconverted pulses. The black curve shows spectral phase measured before the feedback. The second order dispersion is intentionally added to ensure the availability of this feedback system. The second order dispersion was removed quickly by repeating the feedback. The remaining higher order dispersion, especially the fifth order dispersion, was gradually reduced. The blue curve shows measured spectral phase after the 4 times feedback. The pulse duration of this pulse was 27.9 fs, whose Fourier transform limit was 27.3 fs.

2.3 Generation of few-cycle pulses with hollow-core fiber compression technique

Hollow-core fiber technique is used to generate few-cycle pulses. When the intense laser pulse is introduced into the hollow-core fiber, which is filled with rare gas

atoms, non-linear optical effect is enhanced during propagating into the fiber. Self-phase modulation, which is applied to generate white continuum light, is one of the nonlinear optical effect. The time variation of the refractive index n of the medium can be written with linear n_0 and non-linear refractive index n_2 as

$$n = n_0 + n_2 I(t) \qquad (2.12)$$

After propagating in the medium, whose length is l, frequency shift $\delta\omega(t)$ is

$$\delta\omega(t) = -\frac{2\pi n_2 l}{\lambda}\frac{dI(t)}{dt}. \qquad (2.13)$$

The n_2 of rare gas atoms is positive. The frequency of the former part of laser pulse shifts to lower frequencies and that of the latter part shifts to higher frequencies. This means that self phase modulation causes positive group delay dispersion. Fourier transform limit of the laser pulse shortened by adopting this phenomena. To increase the frequency shift, the n_2, l and $I(t)$ can be controlled.

If the pulse duration and pulse energy of the laser system is fixed, the hollow core fiber can be designed with following way. There are two parameters to restrict the design of the hollow core fiber, threshold intensity I_{th} and critical power P_{cr}. When the peak intensity of the laser pulse exceeds the I_{th}, multiphoton ionization process is not negligible. Ionization in the fiber decrease the throughput of the pulse

Table 2.1: Nonlinear refractive indexes and critical power of rare gas atoms.

	He	Ne	Ar	Kr
n_2 (10^{-20} cm^2/W) [3]	0.34	0.85	7.96	18.9
I_{th} (10^{14} W/cm^2)	4 [4]	2 [4]	0.7 [5]	

and degrade the stability. The P_{cr} is given by

$$P_{cr} = \frac{\lambda^2}{2\pi n_2}. \tag{2.14}$$

If the peek power of the laser pulse exceeds the critical power, the laser filament is formed. The filamentaion is also used to generate few-cycle pulses because the laser pulse can propagate with high intensity in the filament. In the hollow core fiber compression, the laser pulse is confined in tiny hole to keep high intensity. The filamentaion is a result of the competition between the Kerr lens effect and Coulomb refocusing. This phenomena may degrade the beam quality after the fiber. The I_{th} and n_2 depend on the species of the medium. Table 2.1 shows n_2 of 1 atm rare gas atoms at 800 nm. First, diameter of the fiber is determined to keep the peak intensity of the pulse lower than the threshold intensity of the medium. The pressure of the medium is limited by the P_{cr}. If the spectrum bandwidth is not enough for the few-cycle pulse, the l should be increased. If the required pulse energy increases, the limitation of the pressure of the medium is harder and longer fiber is necessary.

The hollow core fiber in this study was designed for 4 mJ, 30 fs laser system. The inner diameter of the fiber was set to 330 μm. The optimum beam diameter is 220μm and the intensity is 3.5 $\times$ 10^{14} W/cm^2, which is lower than the I_{th} of Helium. The pressure of the Helium is limited to 2.3 atm. Before designing this hollow core
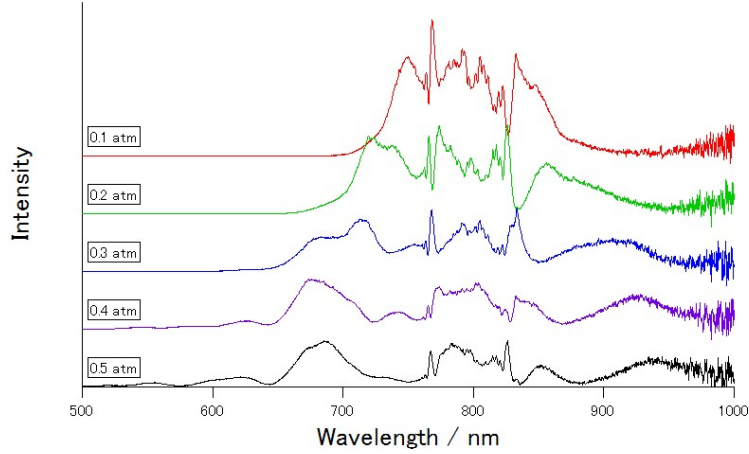
Figure 2.5: Pressure dependence of the spectrum after the hollow core fiber.

fiber, 1 m fiber was tested preliminary. The spectral bandwidth was not enough to generate sub-two-cycle laser pulses. Therefore, 1.5 m fiber was selected to generate few-cycle pulse. For the pump-probe coincidence momentum imaging method, the required pulse energy was around 0.1 mJ. So the input of the fiber was set to 0.6-0.7 mJ and main amplifier of the CPA system was not used.

Figure 2.5 shows pressure dependence of the spectrum after the fiber. The Fourier transform limit decreased to 4.0 fs at 0.5 atm. Spectral phase was compensated with chirped mirrors and wedge plates. The temporal profile of the few-cycle pulses are shown in the next section.

2.4 Characterization of few-cycle pulses with 2DSI and FRAC

Figure 2.6 shows result of 2DSI measurement of few-cycle pulse. Black and blue curve show the spectra of the upconverted pulse and the fundamental pulse, respectively. The ω_1 was adjusted to reproduce the fundamental spectrum. The upconverted spectrum agrees with the fundamental spectrum except the range from 770
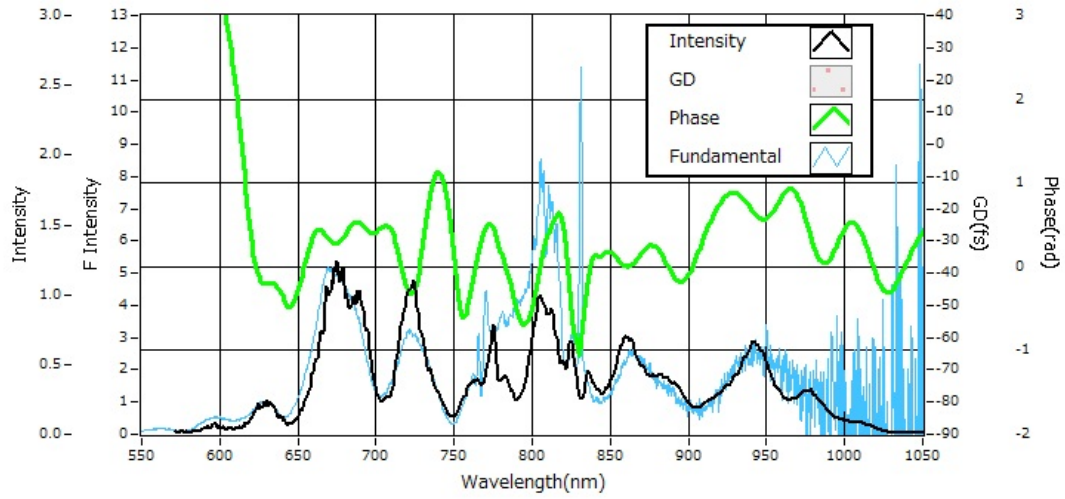
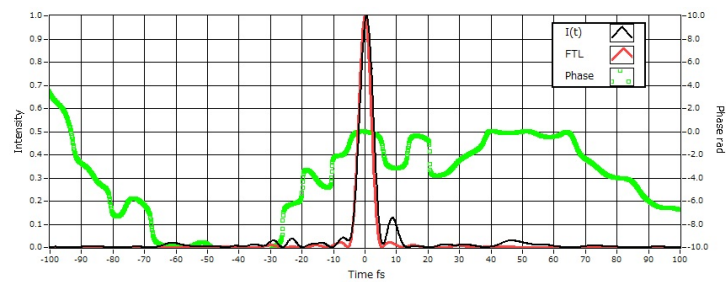Figure 2.6: The spectrum and spectral phase of the few-cycle pulse measured by 2DSI.

Figure 2.7: The temporal shape of few-cycle pulse (black curve) constructed from the result of the 2DSI.
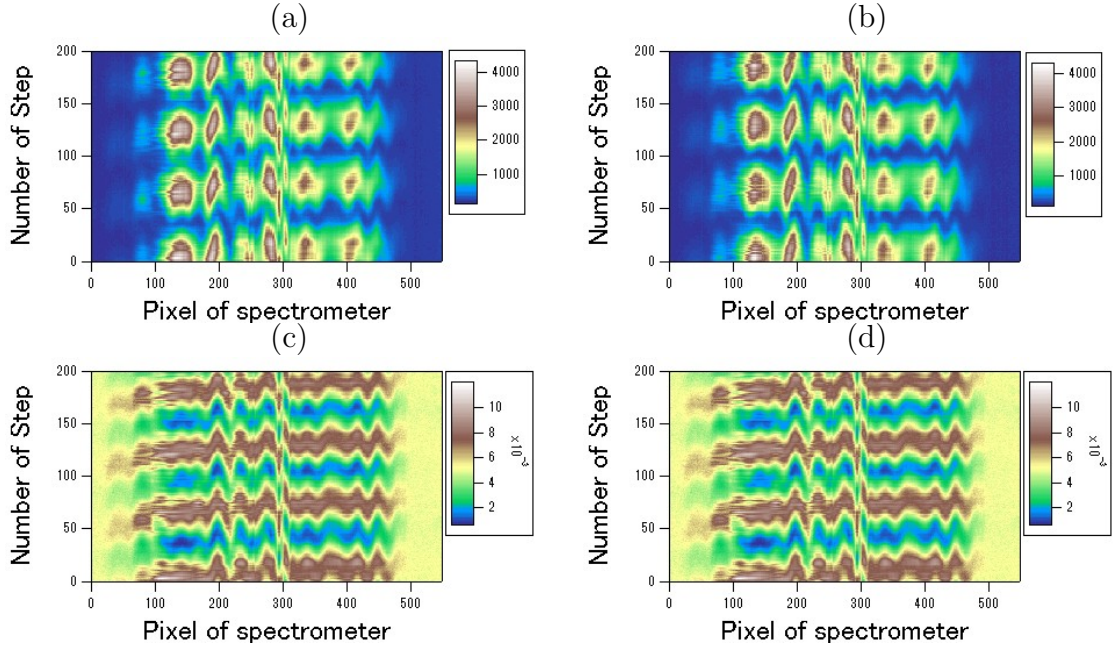
Figure 2.8: (a) The raw data of 2DSI and (b) the raw data of 2DSI after passing through the 1mm fused silica. (c),(d) The normalized 2DSI shown in (a) and (b), to see the interference clearly.

nm to 830 nm. This discrepancy can be caused by amplified spontaneous emission (ASE) of the laser system. The ASE component is not influenced by SPM because temporal coherence is poor and appears in same spectral range after the fiber. The green curve shows the spectral phase measured by 2DSI discussed below. The black curve in Fig. 2.7 shows the temporal shape of the few-cycle pulses obtained from the spectral phase and the spectrum of the upconverted pulse measured by 2DSI. The pulse duration was measured to be 5.0 fs, which is close to the Fourier transform limit (4.6 fs) of the spectra. The temporal shape is represented with the red curve.

The ω_1 was estimated to be $2\pi\cdot$ 349 Thz ($\lambda = 859$ nm) by comparing the fundamental spectrum and upconverted spectrum as shown in Fig. 2.6. The calibration of Ω is important for the few-cycle pulses compared with the measurement of the
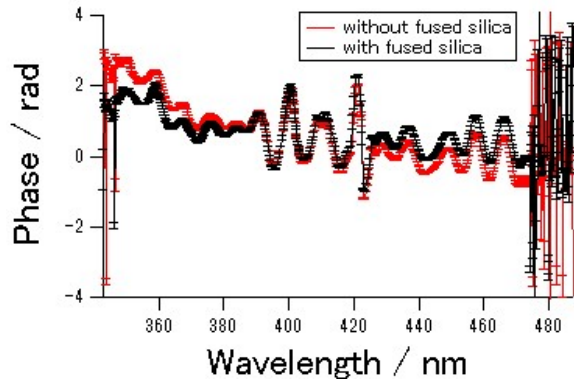
Figure 2.9: The phase term extracted from the raw data of 2DSI.

output of the CPA. The purpose of the measurement of the output of the CPA is to compensate the spectral phase with DAZZLER. The spectral feedback works as long as the estimated shear frequency Ω_{es} is same sign as the Ω and satisfies $|\Omega_{es}| < 2|\Omega|$. The Ω was estimated with a following method. Figure 2.8 (a) and (b) shows raw data of 2DSI. The horizontal axis shows pixel number of spectrometer for the upconverted pulses and vertical axis shows number of steps obtaining the spectra. The interference of the upconverted pulses appears along the vertical direction. The two-dimensional spectra were fitted with cosine function and the phase term include the group delay as discussed before.

Figure 2.9 shows the phase term $\phi(\omega - \omega_1) = \tau_g(\omega - \omega_1)\Omega + \theta_1 - \theta_2$. The difference of these two results should correspond to the group delay of 1 mm fused silica. The Ω was obtained by fitting the difference with the calculated group delay of the fused silica based on the Sellmeier equation as shown in Fig. 2.10. The Ω was obtained to be $2\pi \cdot 3.8$ THz.

Figure 2.11 shows group delay of few-cycle pulses. After inserting the fused silica, the pulse was still negatively chirped. The spectral phase was optimized by
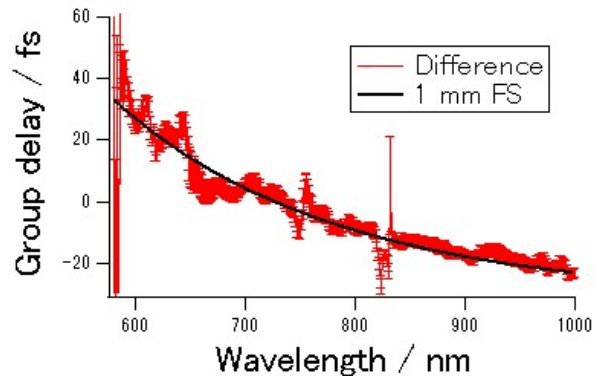
Figure 2.10: The difference of the group delay (red curve) of the few-cycle pulses before and after the 1 mm fused silica.
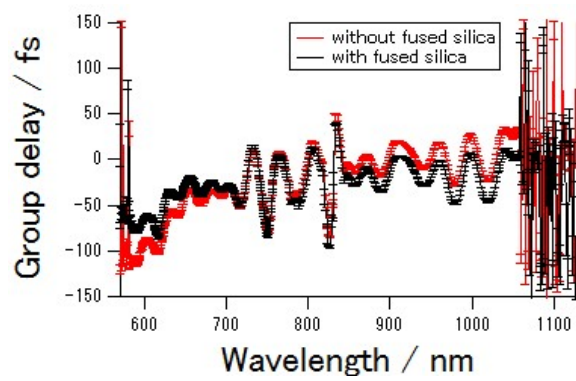

Figure 2.11: The group delay of the few-cycle pulses after the calibration.
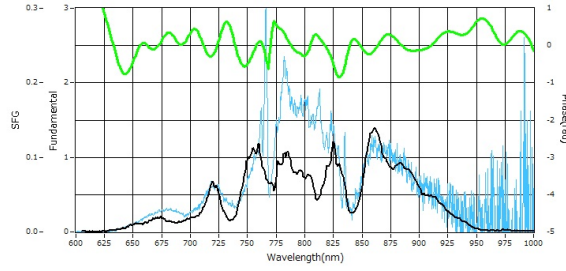
Figure 2.12: The spectrum from the up-converted pulse (black curve), the fundamental spectrum (blue curve) and the spectral phase (green curve) of the few-cycle pulses used for the pump-probe measurement.
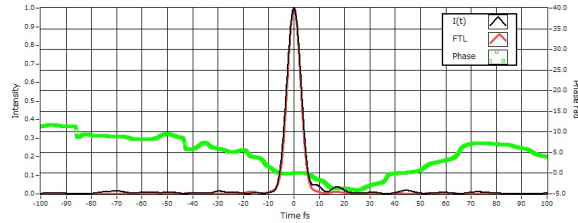
Figure 2.13: The temporal shape of the few-cycle pulse measured by the 2DSI (black curve) and the Fourier transform limited pulse (red curve) used for the pump-probe measurement.

changing the thickness of fused silica virtually and the optimized spectral phase is shown in Fig. 2.6. In the pump-probe coincidence momentum imaging measurement discussed later, the pulse duration was finally optimized by changing the thickness of fused silica to obtain maximum count rate of the ion signal.

By increasing the pressure of Ar gas in the fiber, Fourier transform limit was shortened to be 4.2 fs but the spectral phase was jumped in shorter wavelength region < 650 nm. The shortest pulse duration is 4.9 fs measured by 2DSI. To generate shorter pulse, feasible chirped mirrors should be selected or designed for this spectral phase structure.

Figures 2.12 and 2.13 show the spectrum and the temporal shape of the few-cycle

Figure 2.14: The measured (blue dots) and calculated (red curve) FRAC trace of the few-cycle pulses.
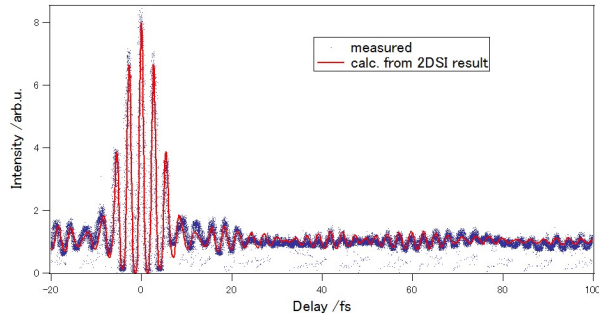
pulse used for the pump-probe experiment. The pulse duration is around 6 fs and the pedestal structure is well-suppressed. The intense few-cycle pulses is frequently used to investigate highly nonlinear processes like high-order harmonics generation, tunnelling ionization and recollision of ionized electron driven by the laser fields. For this propose, the pedestal structure of the laser pulses is not so important because these phenomena occur dominantly in the main part of the laser pulse. On the other hand, the pedestal structure may be important for the fragmentation pathways of the molecules. For this reason, the 5 fs laser pulse was not used for the measurement but the 6 fs pulse with clear pedestal structure.

To confirm the result of 2DSI, fringe resolved second-order autocorrelation (FRAC) was measured and compared with the calculated FRAC trace from the temporal shape of the few-cycle pulses as shown in Fig. 2.14. The blue dots show the intensity of second harmonics in each shot. A $5\mu m$ thickness type I BBO was used to generate second harmonics and the Mickelson interferometer, which was also used for pump-probe experiment to modify the time delay. The calibration of the delay and capturing methods is described in the next chapter. The second harmonics was
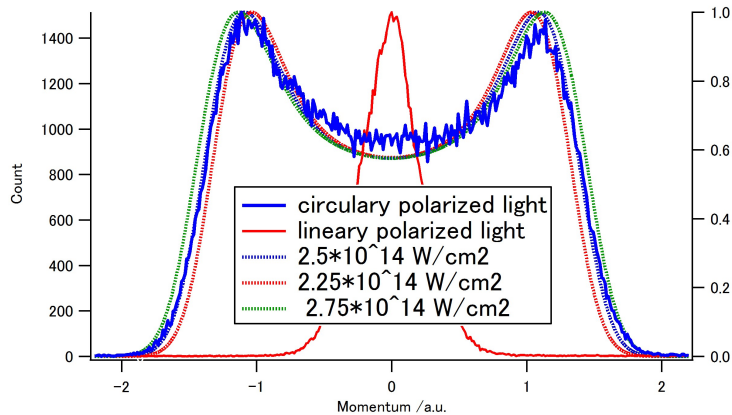
Figure 2.15: The measured recoil momentum distribution of D_2^+ (Blue curve). The dotted lines shows the calculated momentum distributions with respective intensity.

detected by a photo diode and the signal was integrated by a boxcar integrator. The output of the boxcar integrator was connected to a voltage-to-time converter and the output was recorded in a PCI board, which was also used for the CMI measurement.

In the pump-probe experiment, the focal intensity was estimated from the pulse duration, the focal size and the pulse energy. The peak intensity was estimated by another method [6] to confirm that the peak intensity can be estimated from these parameters. The circular polarized few-cycle laser pulses were prepared by using a quarter wave plate. D_2 molecule was irradiated with the circular polarized laser pulses and the momentum distribution of the D_2 was measured. The blue curve in Fig. 2.15 shows the momentum distribution of D_2^+ generated by the circular polarized laser pulse. Dotted lines in Fig. 2.15 show calculated momentum distributions with respective peak intensities. The resolution of the momentum was estimated to the red line, which was obtained by using linearly polarized laser pulses. The experimentally obtained momentum distribution agrees with the calculated distribution

whose peak intensity is $2.5 \times 10^{14} \text{W/cm}^2$. This peak intensity agrees with the peak intensity calculated from the laser parameters.

References

[1] A. Stingl, R. Szipöcs, M. Lenzner, Ch. Spielmann, and F. Krausz. Sub-10-fs mirror-dispersion-controlled Ti:sapphire laser. *Opt. Lett.*, 20:602–604, 1995.

[2] J. R. Birge, R. Ell, and F. X. Kärtner. Two-dimensional spectral shearing interferometry for few-cycle pulse characterization. *Optics Letters*, 31:2063–2065, 2006.

[3] C. Bree, A. Demircan, and G. Steinmeyer. Method for computing the nonlinear refractive index via Keldysh theory. *IEEE Journal of Quantum Electronics*, 46:433–437, 2010.

[4] S. Bohman, A. Suda, T. Kanai, S. Yamaguchi, and K. Midorikawa. Generation of 5.0 fs, 5.0 mj pulses at 1 kHz using hollow-fiber pulse compression. *Optics Letters*, 35:1887–1889, 2010.

[5] M. Nurhuda, A. Suda, K. Midorikawa, M. Hatayama, and K. Nagasaka. Propagation dynamics of femtosecond laser pulses in a hollow fiber filled with argon: constant gas pressure versus differential gas pressure. *The Journal of the Optical Society of America B*, 20:2002–2011, 2003.

[6] A. S. Alnaser, X. M. Tong, T. Osipov, S. Voss, C. M. Maharjan, B. Shan, Z. Chang, and C. L. Cocke. Laser-peak-intensity calibration using recoil-ion momentum imaging. *Physical Review A*, 70:023413, 2004.

3 Pump-probe coincidence momentum imaging

3.1 Introduction

In this chapter, pump-probe coincidence momentum imaging (CMI) method is introduced. The intense few-cycle laser pulse, which is introduced in chap. 2, was focused onto a effusive molecular beam in a ultrahigh vacuum chamber, called CMI chamber. Fragment ions generated by the laser pulses were guided toward a position sensitive detector by static electric fields. Figure 3.1 shows the electrical potential, which can be controlled by applying voltages to electrodes, in this chamber. From the detected position and the flight time of fragment ions, three dimensional momentum image was constructed as described in section 3.2. Fragment ions generated via Coulomb explosion pathway were extracted with CMI method or covariance method. In section 3.3, CMI method and covariance method are introduced. Besides, a new analytical method to estimate a number of event accidentally satisfied momentum matching condition is proposed.

In this pump-probe experiment, delay time between two pulses was controlled by a function generator and the delay time, detected position and flight time were recorded in a PCI board simultaneously. The delay time dependent momentum distribution of the fragment ions was constructed by sorting the data after the accumulation. This method is described in section 3.4.
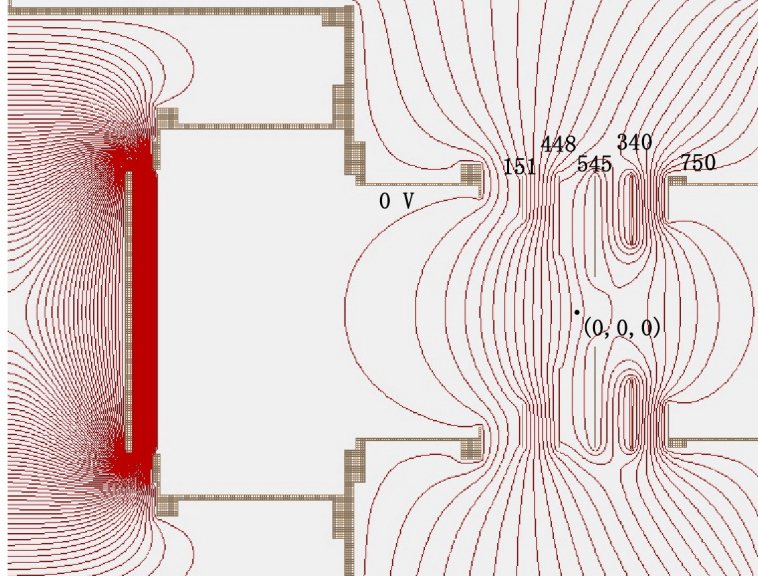
Figure 3.1: Electric potential in the CMI chamber.

3.2 Momentum of fragment ions

Figure 3.1 shows the electric potential in the ultrahigh vacuum chamber used for the experiment. The voltage of rhe electrode is shown in the Fig. 3.1 and set to project the momentum of fragment ions, which are generated at (0,0,0) shown in the Fig. 3.1, on the time and position sensitive detector composed of MCP and delay-line anode. From the flight time t and position $\vec{x} = (x, y)$, the three dimensional momentum $\vec{p} = (p_x, p_y, p_z)$ was obtained as

$$p_x(t', x) \quad = \quad x \sum_{n=0}^{4} c_n(t')^n + x^3 \sum_{n=0}^{3} d_n(t')^n, \tag{3.1}$$

$$p_y(t', y) \quad = \quad y \sum_{n=0}^{4} c_n(t')^n + y^3 \sum_{n=0}^{3} d_n(t')^n, \tag{3.2}$$

$$p_z(t', x, y) \quad = \quad \sum_{n=1}^{5} a_n(t')^n + (x^2 + y^2) \sum_{n=0}^{5} b_n(t')^n, \tag{3.3}$$

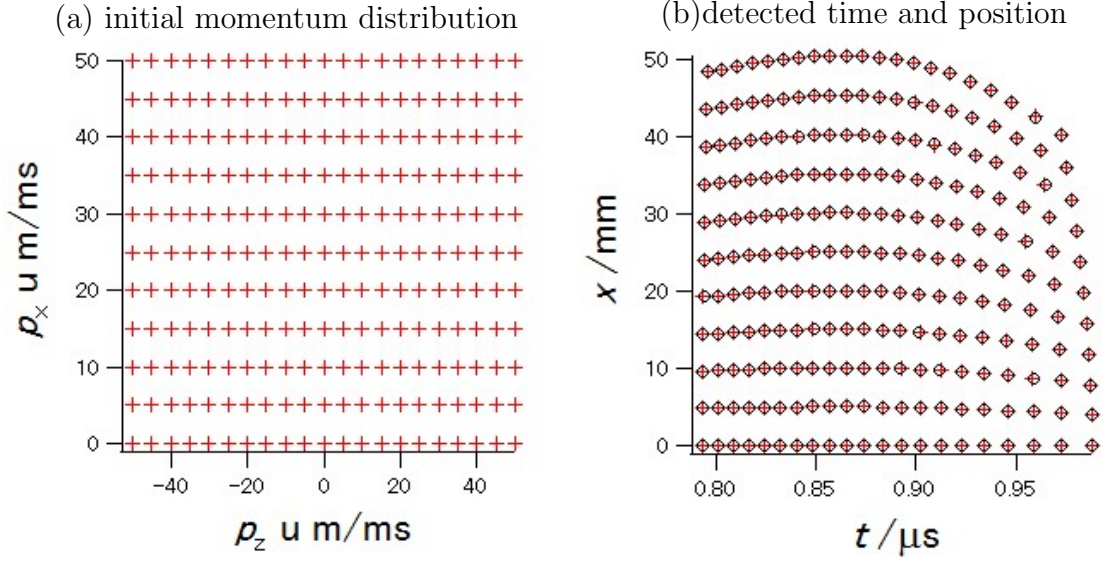$$t' \quad = \quad t - t_0, \tag{3.4}$$

Figure 3.2: Momentum to flight time and the x.

where t_0 is the flight time of the fragment ion which has no momentum. The coefficients for the polynomials were determined by using SIMION 8.0. The trajectory and detected time of fragment ions, which lunched at $(0, 0, 0)$ with initial momentum as shown in Fig. 3.2 (a), were calculated by using SIMION 8.0. The initial momentum was scanned along p_x and p_x to determine the coefficients. The detected time and and the position x are plotted on Fig. 3.2 (b) as cross-hairs. The coefficients were determined by a least square method and the results of the fitting are shown as open circle. The fitting plot reproduces the t and the x well. By using these coefficients, the momentum distribution of H_3^+ generated from methanol molecules via Coulomb explosion was obtained in order to confirm that the coefficients can be used.

Figure 3.3 shows the distribution of H_3^+ respect to the x and the t. The wavelength of the laser pulses was sub-μm and the electric dipole approximation can be
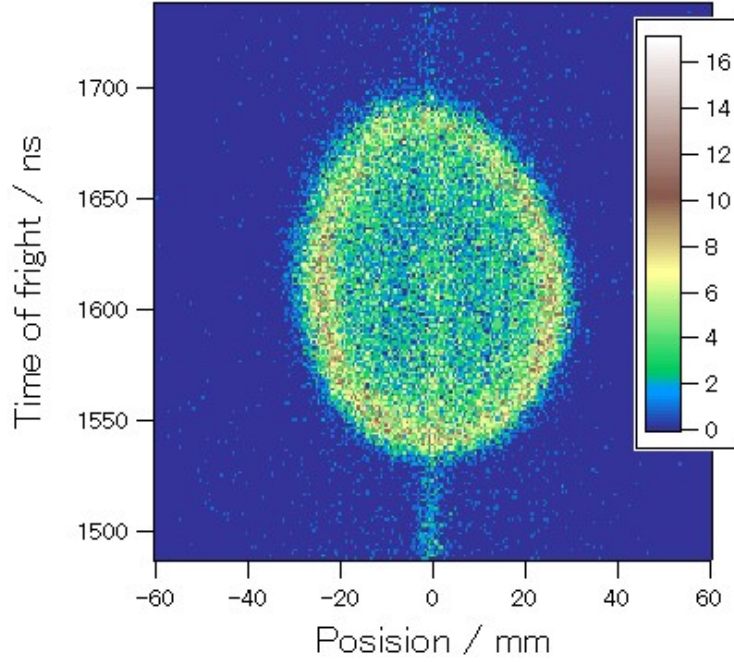
Figure 3.3: distribution of H_3^+ along the t and x.

applied. Under the approximation, the momentum distribution should have a cylindrical symmetry along the polarization direction. This means that the momentum distribution in $x - z$ plane should be cylindrical.

Figure 3.4 (a) shows momentum distribution of H_3^+ obtained from the raw data shown in Fig. 3.3 and the coefficients. The momentum distribution along the p_z direction is narrower than the p_x direction. It is considered that the originating position of fragment ions was shifted from the designed position. The focal position of the laser pulses was optimized to maximize the number of signal detected by the MCP. If the sample beam is shifted from the designed position, the originating position should be shifted. The originating position was changed to obtain cylindrical momentum distribution. When the originating position was set to (0,0,3), the cylindrical distribution was obtained as shown in Fig. 3.4 (b). The coefficients
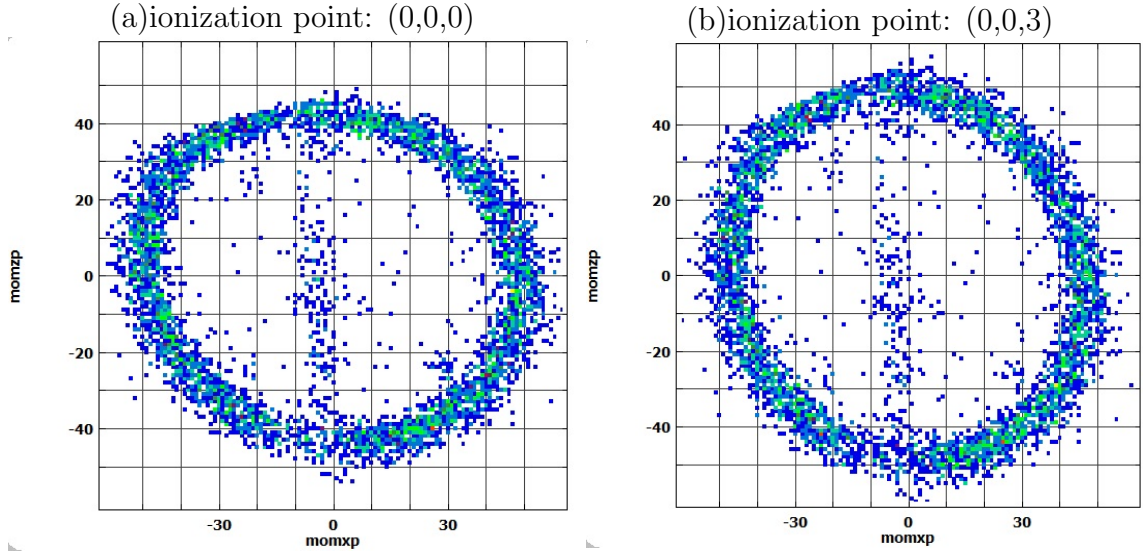
36

Figure 3.4: Momentum distribution of H_3^+.

calculated from (0,0,3) were used to convert the (x, y) and the t to (p_x, p_y, p_z).

3.3 Data analysis

The momentum of fragment ions generated by irradiating intense laser pulses into molecule has an information how the fragment ions generated. In order to investigate the decomposition pathway of multiple charged ions, coincidence measurement and covariance method are used [1]. When multiple charged ions are decomposed into the fragment ions, CMI method is useful. When doubly charged ions are generated by the laser pulse, the ions can be decomposed into two fragment ions with relatively higher momentum. This decomposition process is called Coulomb explosion. The sum of the momentum of the fragment ions, which are decomposed from the doubly charged ion via Coulomb explosion, should conserve the momentum of the doubly charged ion. The momentum distribution of the doubly charged ions can be approximated to the initial momentum distribution of the sample effusive

gas. In the CMI method, the ion pare, whose total momentum is close to the initial momentum, is extracted.

When the several molecules are generated by one laser pulses, the fragment ions which generated from different molecules accidentally satisfy the momentum matching condition, which is called false coincidence. To reduce the false coincidence event, the signal rate is reduced to ~ 1 event/pulse, that is, only one ion are generated by focusing a laser pulse. It is known that the small momentum component in the coincidence momentum map corresponds to the false coincidence event, whereas the number of false coincidence events did not estimated. In the previous study [2] in CH_3OD_3 molecule, the method to estimate number of false coincidence events was proposed. They mentioned number of false coincidence events can be estimated from the momentum distribution of the ions generated by other laser pulses. They also mentioned that their method can overestimate number of false coincidence events. By comparing the definition of covariance and coincidence measurement, a new estimation method is proposed in this section and the validity of this method is shown by a simulation.

The definition of covariance can be written as

$$
\begin{aligned}
\mathrm{cov(A, B)} &= \langle (A - \langle A \rangle)(B - \langle B \rangle) \rangle \\
&= \langle AB \rangle - \langle A \rangle \langle B \rangle
\end{aligned}
\tag{3.5}
$$

where A and B show the signals of interest [1]. The physical meaning of first term is the probability that A and B are detected simultaneously and the second term

means the probability that A and B are detected simultaneously without correlation. By subtracting second term from first term, correlated signal can be extracted.

Ideally, coincidence measurements performed under the condition that the false coincident event is significantly negligible by reducing number of signals observed in each laser shot. In this condition, the second term of covariance is negligible and the relationship between number of coincidence events and covariance is written as

$$\mathrm{coinc(A, B)} \approx N\mathrm{cov(A, B)}. \tag{3.6}$$

The N represents number of laser shots. Covariance can be obtained as a function of any parameters. To apply this covariance method for the fragment ions, the one dimensional momentum of ion A and B is set as a parameter.

$$\mathrm{cov}(\mathrm{A}(p_A), \mathrm{B}(p_B)) = \langle \mathrm{A}(p_A)\mathrm{B}(p_B) \rangle - \langle \mathrm{A}(p_A) \rangle \langle \mathrm{B}(p_B) \rangle \tag{3.7}$$

$$\langle \mathrm{A}(p_A)\mathrm{B}(p_B) \rangle = \frac{1}{N} \sum_{i=0}^{N} \delta(p_A - p_A^{(i)})\delta(p_B - p_B^{(i)}) \tag{3.8}$$

$$\langle \mathrm{A}(p_A) \rangle = \frac{1}{N} \sum_{i=0}^{N} \delta(p_A - p_A^{(i)}) \tag{3.9}$$

This is called covariance mapping method. $p_A^{(i)}$ represents the momentum of ion A obtained with i-th laser shot. The delta function returns zero if ion A is not observed.

By applying momentum matching condition to the covariance of ion A and B,

number of true coincidence events can be obtained as

$$
\begin{aligned}
\mathrm{CMI(A,B)} &= \iint \mathrm{coinc}(\mathrm{A}(p_A), \mathrm{B}(p_B))w(p_A + p_B)dp_A dp_B \\
&= N \iint \langle \mathrm{A}(p_A)\mathrm{B}(p_B)\rangle w(p_A + p_B)dp_A dp_B \\
&\quad -N \iint \langle \mathrm{A}(p_A)\rangle\langle \mathrm{B}(p_B)\rangle w(p_A + p_B)dp_A dp_B \\
&= \sum_{i=0}^{N} w(p_A^{(i)} + p_B^{(i)}) - \frac{1}{N}\sum_{i=0}^{N}\sum_{j=0}^{N} w(p_A^{(i)} + p_B^{(j)}) \qquad (3.10)
\end{aligned}
$$

$$
N_m = \sum_{i=0}^{N} w(p_A^{(i)} + p_B^{(i)}) \qquad (3.11)
$$

$$
N_{ef2} = \frac{1}{N}\sum_{i=0}^{N}\sum_{j=0}^{N} w(p_A^{(i)} + p_B^{(j)}) \qquad (3.12)
$$

The w represents a window function to extract momentum-matched ion pares. The first term in Eq. 3.10 shows the number of coincidence events N_m used in previous studies. The second term corresponds to the number of estimated false coincidence events N_{ef2} in CMI method proposed in this study. This term is different from that proposed in the previous study [2]. In the previous study, the number of false coincidence events was estimated as

$$
N_{ef1} = \frac{1}{N_c - 1}\sum_{i=0}^{N_c}\sum_{j\neq i}^{N_c} w(p_A^{(i)} + p_B^{(j)}) \qquad (3.13)
$$

$$
N_c = N\langle \mathrm{AB}\rangle \qquad (3.14)
$$

where N_c represents the number of the events, in which ion A and B are observed simultaneously. In the previous method, the window function was applied after extracting the ion pares which are detected at a time. In order to compare these
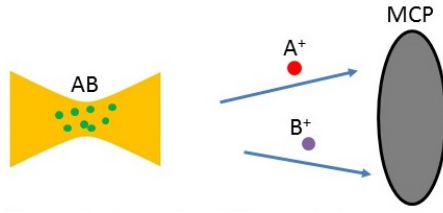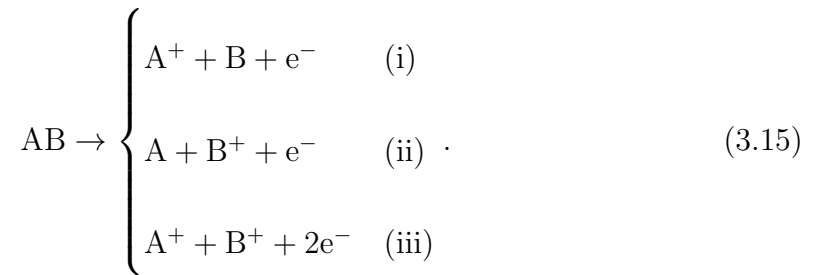
Figure 3.5: Model for the comparison between N_{ef1} and $N_{N_{ef2}}$.

two method, I simulated number of true coincidence, false coincidence and estimated false coincidence events in the condition described below. I assumed that 100 molecules "AB" can interact with each laser pulse and "AB" can be decomposed with certain probabilities through following pathways:

$$
AB \rightarrow
\begin{cases}
A^+ + B + e^- & \text{(i)} \\
A + B^+ + e^- & \text{(ii)} \\
A^+ + B^+ + 2e^- & \text{(iii)}
\end{cases}
\cdot
\tag{3.15}
$$

In the pathways (i) and (ii), the momentum distribution of generated ions was set to 0 ± 10. In the pathway (iii), it was assumed that $p_A = -p_B = 40 \pm 10$. The probabilities of these pathways were set as initial conditions. The generated ions were detected by a MCP, whose detection efficiency is 50% as shown in Fig. 3.5. After detecting the ions, momentum matching condition, $|p_A + p_B| < 1$ arb. u., was applied. The results are shown in Tables 3.1 and 3.2. The N_{ef2} agrees with the N_f in present method under the all conditions as shown in table 3.2. In the previous method, the N_{ef1} agrees with the N_f under the conditions 1 and 2, which have no Coulomb explosion pathways. However, in the conditions 3 and 4, which have only

Table 3.1: The result of simulation of number of false coincidence estimated with previous method (N=100000).

Conditions	(i) (%)	(ii) (%)	(iii) (%)	N_c	N_m	N_t	N_f	N_{ef1}	$\frac{N_C}{N}N_{ef1}$
1	0.1	0.1	0	217	7	0	7	11.6	
2	0.2	0.2	0	886	42	0	42	48.9	
3	0	0	0.25	5447	5171	5165	6	152.2	8.3
4	0	0	0.5	9693	8639	8613	26	274.2	26.6

Table 3.2: The result of simulation of number of false coincidence estimated with present method (N=10000).

Conditions	(i) (%)	(ii) (%)	(iii) (%)	N_m	N_t	N_f	N_{ef2}
1	0.5	0.5	0	37	0	37	34.9
2	1	1	0	128	0	128	139.5
3	0	0	0.5	1291	1273	18	18.0
4	0	0	1	2586	2511	75	71.1

the Coulomb explosion pathway, number of false coincidence events is overestimated as shown in Table 3.1.

In the previous study, it was mentioned that the previous method can estimate number of false coincidence events when there are no correlations and that the previous method overestimate the number of false coincidence events. The covariance mapping method has one problem to applying for measurements. It is known that the covariance method overestimate if some laser parameters are fluctuating and the probability of decomposition pathways depends on the parameters. For example, 50 % of laser pulses is significantly weak and no ions are generated, N_{ef2} decreases to 50 %. The covariance mapping method is often used in free electron laser (FEL) facility and the output spectrum and intensity of self-amplified spontaneous emission FEL is fluctuated by shot to shot. One of the method to reduce the effect of

fluctuations of laser parameter is partial covariance method [3]. It can be written as

$$\mathrm{pcov}(\mathrm{A},\mathrm{B};I) = \mathrm{cov}(\mathrm{A},\mathrm{B}) - \frac{\mathrm{cov}(\mathrm{A},I)\mathrm{cov}(I,\mathrm{B})}{\mathrm{cov}(I,I)}. \tag{3.16}$$

The I represents one of the parameters of the laser pulses, for example, intensity of the pulses. In my study, the effect of fluctuations of laser parameter was reduced by using following definition of number of estimated false coincidence events as

$$N_{ef3} = \sum_{i=0}^{N} w(p_A^{(i)} + p_B^{(i+1)}) \tag{3.17}$$

This estimation method can reduce the effect of laser fluctuation by comparing the momentum of fragment ions generated by neighbouring laser pulses. It is considered that the main origin of laser instability is mechanical vibration of the optics and the optical tables in the laser system. The typical vibration frequency is less than 100 Hz. It is considered that the difference of neighbouring laser pulses is quite small because the repetition rate of the laser system (5 kHz) is much higher than the vibration frequency.

A factor for underestimation also exists. The dead time of the detector was not considered in this estimation. Once the ions are detected, the detector can not work for the order of 100 ns after the detection. However, the N_{ef2} is not zero even if the difference between the detected time of ion A and B is less than 100 ns. The dead time of the detector can cause the underestimation of the correlation.
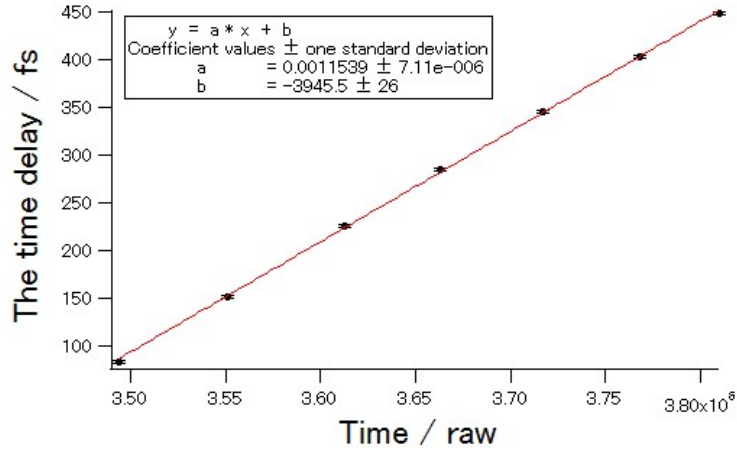
Figure 3.6: Calibration of the delay.

3.4   Pump-probe setup

In the pump-probe CMI measurement, the pump and probe laser pulses were pre-
pared by using the Michelson interferometer and the time delay was controlled with
the piezo stage. The piezo stage was scanned by using the function generator and
the position was measured by a piezo strain gauge reader. The output of the reader
(voltage: 0sin10 V) was converted to the time by using a home-made electric circuit.
The time was recorded in a PIC board (TDC8 HP, Roentdeck). Figure 3.6 shows
the relationship between the time and the time delay. The time delay was calculated
from the output spectrum of the interferometer. The interference between the pump
and probe pulses appears in spectral region. The delay can be determined from the
Fourier transform of the interfered spectrum. The time delay was obtained by using
the coefficients as shown in the inset of Fig. 3.6.

References

[1] L. J. Frasinski, K. Codling, and P. A. Hatherly. Covariance mapping: a correlation method applied to multiphoton multiple ionization. *Science*, 246:1029–1031, 1989.

[2] R. Kanya, T. Kudou, N. Schirmel, S. Miura, K. M. Weitzel, K. Hoshina, and K. Yamanouchi. Hydrogen scrambling in ethane induced by intense laser fields: Statistical analysis of coincidence events. *The Journal of Chemical Physics*, 136:204309, 2012.

[3] L. Frasinski, V. Zhaunerchyk, M. Mucke, R. Squibb, M. Siano, J. Eland, P. Linusson, P. v.d. Meulen, P. Salén, R. Thomas, M. Larsson, L. Foucar, J. Ullrich, K. Motomura, S. Mondal, K. Ueda, T. Osipov, L. Fang, B. Murphy, N. Berrah, C. Bostedt, J. Bozek, S. Schorb, M. Messerschmidt, J. Glownia, J. Cryan, R. Coffee, O. Takahashi, S. Wada, M. Piancastelli, R. Richter, K. Prince, and R. Feifel. Dynamics of hollow atom formation in intense X-ray pulses probed by partial covariance mapping. *Physical Review Letters*, 111:073002, 2013.

4 Wave packet bifurcation in ultrafast hydrogen migration in CH_3OH^+ by pump-probe coincidence momentum imaging with few-cycle laser pulses

4.1 Introduction

Our recent studies [1–5] have revealed that ultrafast hydrogen migration processes are induced in hydrocarbon molecules when they are irradiated with ultrashort intense laser pulses. In all the cases of CH_3CN [1], CH_3OH [2] and C_3H_4 (allene) [3] [4], hydrogen migration processes were induced efficiently by the irradiation of femtosecond laser pulses whose pulse durations were ranged between 40 and 70 fs. In these studies, however, it remained unclear whether the migration proceeded in the singly or higher charged parent species, because the hydrogen migration within a parent molecule and its multiple ionization were both induced within the duration of the laser pulses.

In 2010, we investigated the hydrogen migration in CH_3OH at real time by measurements of pump-probe coincidence momentum imaging (CMI) using femtosecond laser pulses whose duration was 38 fs, and we were able to find that the hydrogen migration proceeds in CH_3OH^+, and that there are two different time scales in the hydrogen migration: (i) faster hydrogen migration having completed already at the shortest pump-probe time delay at 100 fs and (ii) slower hydrogen migration with

a time constant of ~150 fs [5]. In order to investigate how fast the faster hydrogen migration proceeds, it was necessary to use much shorter laser pulses in the pump-probe measurements.

In the present study, we have generated few-cycle laser pulses with pulse durations as short as 6 fs, and by using the few-cycle laser pulses, we have performed pump-probe CMI measurements of hydrogen migration processes in CH_3OH^+. We have thus detected the fragment ions produced by the following two Coulomb explosion pathways:

Non-migration pathway

$$CH_3OH^{2+} \rightarrow CH_3^+ + OH^+, \tag{4.1}$$

Migration pathway

$$CH_3OH^{2+} \rightarrow CH_2^+ + OH_2^+, \tag{4.2}$$
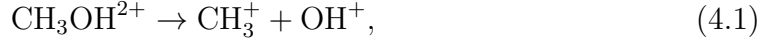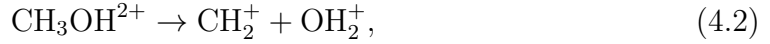
and recorded the distribution of the released kinetic energies as a function of the pump-probe time delay ranging between -20 and 500 fs.

For the non-migration pathway, we find that the C-O bond breaking,

$$CH_3OH^+ \rightarrow CH_3^+ + OH, \tag{4.3}$$

proceeds via the energized states in the first electronically excited $\tilde{A}$ state. For the migration pathway, we have found that a nuclear wave packet flows from the higher electronic states than the $\tilde{A}$ state in the non-migrated geometrical configuration into

the bound well of the migrated geometrical configuration, and oscillates first along the C-O bond, and then bifurcates at ∼150 fs into the bound component and the dissociative component that leads to the C-O bond breaking,

$$CH_3OH^+ \rightarrow CH_2^+ + H_2O. \tag{4.4}$$

4.2 Experimental

The experimental setup for the generation of linearly polarized few-cycle laser pulses and the detection of fragment ions have been described previously [6]. The experimental setup consists of (i) a chirped-pulse-amplification femtosecond Ti:sapphire laser system, (ii) a pulse compression system to generate few-cycle laser pulses [7] and (iii) an ultrahigh vacuum chamber for CMI measurements [8]. Output pulses of the femtosecond laser system (800 nm, 5 kHz, 0.6 mJ, 30 fs) were focused into a hollow-core fiber (1.5 m long, 330 μm inner diameter) filled with an Ar gas (0.4 atm) to induce the self-phase modulation. After passing through the fiber, the spectral bandwidth of the laser pulses became ∼ 300 nm at full-width at tenth-maximum at the center wavelength of 770 nm. The spectral phase dispersion was compensated by chirp mirrors (PC70, Ultrafast Innovations) and a pair of wedged fused silica plates for few-cycle laser pulses, which were characterized by a home-built two-dimensional spectral shearing interferometer [9]. The few-cycle laser pulses were then introduced into a Michelson interferometer to generate pump and probe laser pulses, and the optical time delay Δt of a probe laser pulse measured from a pump laser pulse was

varied using a piezo-controlled optical stage. The pulse duration were measured to be 6.0(5) fs. The piezo stage is controlled by a function generator and Δt is scanned from -20 fs to 500 fs at 0.01 Hz to cancel out the effect of long term fluctuations in the sample gas density as well as in the spatiotemporal profile of laser pulses. The pump and probe laser pulses were both focused by a concave mirror ($f = 150$ mm) placed in the vacuum chamber onto an effusive molecular beam of methanol (CH_3OH) vapor, whose rotational temperature is estimated to be the same as room temperature. The polarization directions of pump and probe laser pulses were set to be parallel to the propagation axis of the molecular beam.

The fragment ions generated from CH_3OH were guided by a static electric field toward a two-dimensional position sensitive detector (HEX120, RoentDek) in the velocity map imaging configuration. The momentum vectors of the fragment ions were determined from the flight time and the positions of the fragment ions. For every laser shot, the momentum data of the fragment ions and the delay time data were collected simultaneously by a data acquisition board (TDC8HP, RoentDek). By imposing coincidence conditions on the momentum and delay time data, two-body Coulomb explosion pathways (1) and (2) were extracted, and the released kinetic energies obtained from the momenta of fragment ion pairs were plotted as a function of Δt. The laser field intensity at the focal spot was estimated to be 2.1(2) x 10^{14} W/cm^2 from the pulse energy, pulse duration and focal spot size.
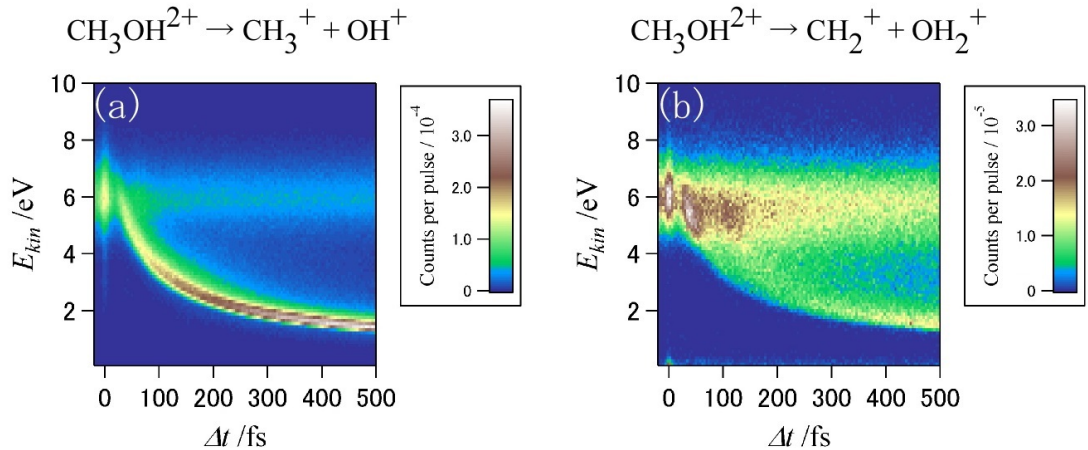
$$CH_3OH^{2+} \rightarrow CH_3^+ + OH^+ \qquad CH_3OH^{2+} \rightarrow CH_2^+ + OH_2^+$$

Figure 4.1: The E_{kin} distributions in the non-migration pathway (a) and the migration pathway (b) as a function of Δt. The number of the counts in each time bin whose width is 4 fs is normalized by the total number of the laser shots in the bin. The width of the time bin is set to be slightly shorter than the laser pulse duration ($\sim$6 fs).

4.3 Results and discussion

4.3.1 Extraction of pump-probe signals

Figure 4.1(a) and (b) shows the distributions of the released kinetic energy E_{kin} as a function of Δt in the Coulomb explosion pathways (4.1) and (4.2), respectively. These E_{kin} distributions also include contributions from the signals generated only by pump laser pulses and those only by probe laser pulses. This is because methanol dications (CH_3OH^{2+}) can also be generated by a single pulse and the fragment ions can be produced by the Coulomb explosion processes of CH_3OH^{2+}. In order to subtract the effect of this single pulse double ionization, the E_{kin} distributions were measured using only pump laser pulses or probe laser pulses. The results are shown in Figigure 4.2(a) and (b) for the non-migration pathway (4.1) and the migration pathway (4.2), respectively.
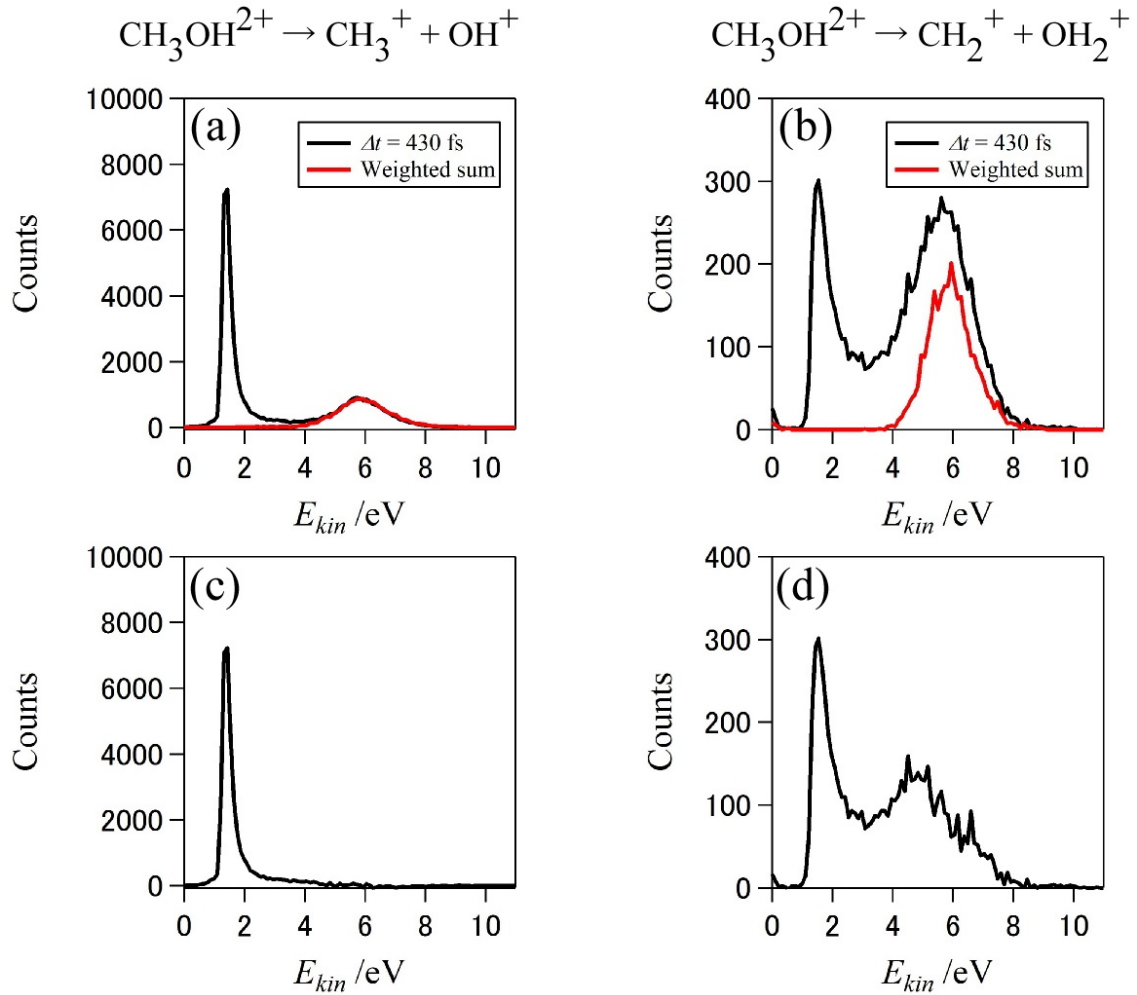
Figure 4.2: The E_{kin} distributions of the non-migration pathway ((a) and (c)) and the migration pathway ((b) and (d)). In (a) and (b), the E_{kin} distributions obtained when $\Delta t = 430$ fs (black curve) and the weighted sum of the kinetic energy distribution obtained with the pump laser pulses only and that obtained with probe laser pulses only (red curve) are shown. In (c) and (d), the E_{kin} distributions obtained by subtracting the weighted sum from the E_{kin} distributions obtained when $\Delta t = 430$ fs are shown.

In the pump-probe measurements, after a pump laser pulse ionizes molecules in a sample gas, the number of neutral molecules decreases to a certain extent. If the number of neutral molecules N within the interaction volume decreases to αN ($\alpha < 1$), the yield of doubly ionized molecules produced by a probe laser pulse should also decrease by a factor of α in comparison to the yield of the doubly ionized molecules generated by a pump laser pulse. In order to account for this depletion effect induced by the pump laser pulses in the pump-probe measurements, the red curves in Figure 4.2(a) and (b) were obtained as a weighted sum of the ion yields defined as

$$I_{\text{weighted}} = I_{\text{pump}} + \alpha I_{\text{probe}} \qquad (4.5)$$

where I_{pump} represents the total yield of ions generated by the pump laser pulses only and I_{probe} represents the total yield of the ions generated by the probe laser pulses only. Under the present experimental conditions, the factor α was estimated to be 0.79(5) as the averaged value of α obtained by the two separate sets of the measurements of the total ion yields obtained by (i) pump laser pulses only, (ii) probe laser pulses only, and (iii) pump and probe pulses with $\Delta t = 430$ fs.

Figures 4.2(c) and (d) shows respectively the E_{kin} distributions of the non-migration pathway and the migration pathway obtained by subtracting the weighted sum of the E_{kin} distribution from the E_{kin} distribution obtained by the pump-probe experiment when $\Delta t = 430$ fs. Therefore, the E_{kin} distributions in Figure 4.2(c) and (d) can be regarded as those originating from the sequential ionization processes by pump and probe laser pulses. As shown in Figure 4.2(c), in the non-migration path-

way, the peak appearing at 6 eV in the pump-probe measurement disappears almost completely, and only the very weak tail region extending from the peak appearing at 2 eV can be identified. In the migration pathway shown in Figure 4.2(d), on the other hand, two distribution peaks with a relatively sharp distribution centered at 2 eV and with the broad distribution at 4.5 eV, can be clearly identified. For the E_{kin} distributions recorded at different delay times, we made the same analysis and extracted the E_{kin} distributions originating from the sequential ionization, as plotted in the two-dimensional maps shown in Figure 3(a) and (b) for the non-migration and migration pathways, respectively.

4.3.2   Time dependent kinetic energy release distributions in Coulomb explosion pathways

In the E_{kin} distribution in Figure 4.3(a), only one distinct component displaying a monotonic decrease in the peak positions with the increases in the pump-probe delay can be identified. To the contrary, two distinct components can be identified in Figure 4.3(b): (i) the component having the higher E_{kin} at ∼4.5 eV exhibits a broad distribution with a characteristic periodical structure peaked at 35, 120, and 200 fs, and (ii) the component having the lower E_{kin} starts to appear at ∼150 fs and decreases monotonically as the pump-probe delay increases.

When the C-O distance in CH_3OH^+ increases, the kinetic energy released by the Coulomb explosion, $CH_3OH^{2+} \rightarrow CH_3^+ + OH^+$, occurring immediately after the ionization into CH_3OH^{2+} from CH_3OH^+ by a probe laser pulse, decreases. Therefore, the E_{kin} distribution shown in Figure 4.3(a) can be interpreted as the motion

$CH_3OH^{2+} \rightarrow CH_3^+ + OH^+$

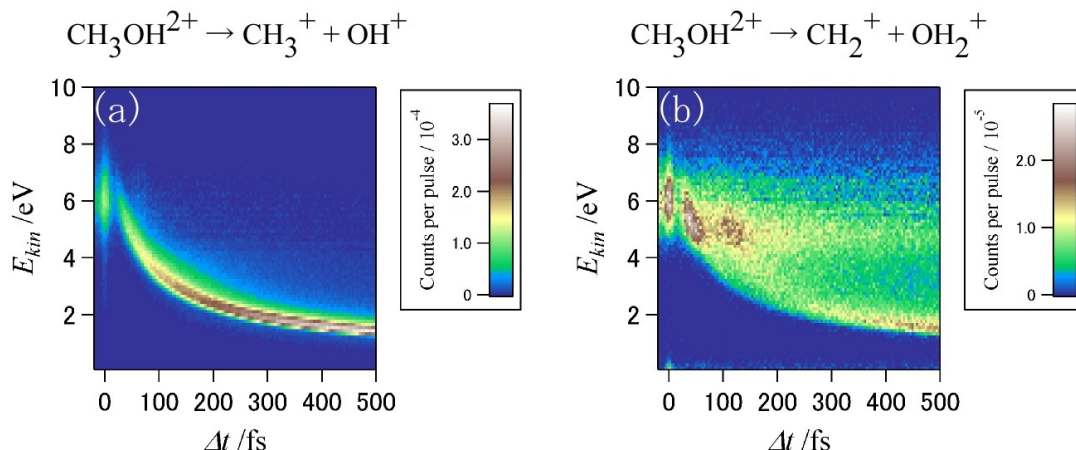$CH_3OH^{2+} \rightarrow CH_2^+ + OH_2^+$

Figure 4.3: The E_{kin} distributions in the non-migration pathway (a) and the migration pathway (b) as a function of Δt obtained after subtracting the effect of single pulse double ionization. The number of the counts in each time bin whose width is 4 fs is normalized by the total number of the laser shots in the bin. The width of the time bin is set to be slightly shorter than the laser pulse duration ($\sim$6 fs). In both (a) and (b), the intense and narrow distribution appearing at $\Delta t = 0$ stretching in the kinetic energy range between 5.3 and 6.7 eV is ascribed to the non-linearly increased ion signals that were not subtracted by the subtraction correction.

of a nuclear wave packet, which is prepared on the potential energy surface (PES) of CH_3OH^+ by a pump laser pulse, along the C-O bond. The two distinct components in Figure 4.3(b) are considered to reflect two different types of nuclear dynamics in the migrated geometry, $CH_2OH_2^+$. The lower E_{kin} component starts to appear at 120 fs and its E_{kin} decreases as the pump-probe delay increases. This lower E_{kin} component can be assigned to the dissociative motion of a wave packet along the C-O bond into $[CH_2 \cdots OH_2]^+$, which dissociates into $CH_2^+ + H_2O$. On the other hand, the higher E_{kin} component exhibiting the characteristic oscillatory structures can be assigned to the motion of a vibrational wave packet trapped in the bound potential at the migrated geometrical structure, $CH_2OH_2^+$ [5]. The delay-time dependences of these two components show that the wave packet prepared by a pump

laser pulse vibrates until $\sim$120 fs, and then bifurcates into two components: one component continuing the vibration in the bound well and the other dissociating along the C-O coordinate.

In the higher E_{kin} component, the first intense area appearing in the delay time ranging between 25 and 60 fs exhibits a nearly vertical but slightly tilted structure; that is, the E_{kin} drops from 6.0 eV at $\Delta t = 25$ fs to 4.9 eV at $\Delta t = 60$ fs. The second and broader intense area appearing in the delay time ranging between 90 and 140 fs exhibits a shallower slope than the first intense area, and the lowest E_{kin} edge of this distribution is smoothly connected to the lower E_{kin} component whose E_{kin} decreases monotonically. In the delay time ranging between 160 fs and 220 fs, the third intensity maximum exhibiting the distribution stretching along the time axis can be identified, though its intensity is approximately a half of the second intense area.

The first and second intense areas in Figure 4.3(b) in the higher E_{kin} component can be interpreted in terms of the temporal variation of the C-O distance in $CH_2OH_2^+$. The first peak shows that the wave packet migrates into the potential valley of the hydrogen migrated configuration from the non-migrated configuration at $\Delta t = 25$ fs, and into C-O distance increases as time elapses and takes the longest distance at $\Delta t = 60$ fs. Then, the C-O distance starts decreasing until $\Delta t = 90$ fs, and starts increasing again toward the longer C-O distance with a speed slower than in the first peak. These first two peaks clearly show that the C-O stretching vibrational motion proceeds in the bound part of the potential of the migrated species $CH_2OH_2^+$. The bifurcation at $\sim$150 fs indicates that a part of the oscillating

wave packet starts escaping from the bound configuration into the dissociation valley, leading eventually to the formation of two fragments, CH_2^+ and H_2O, and the remaining part of the wave packet left in the bound part is bounced back to keep its oscillation.

In the non-migration pathway, a high E_{kin} component similar to the one identified in the migration pathway could not be seen. A wave packet prepared by the pump laser pulse on the bound part of the PES of methanol cation, CH_3OH^+, at the non-migrated configuration is also expected to oscillate along the C-O bond. However, because the wave packet oscillating in the bound well of CH_3OH^+ is considered to be transferred to the quasi-bound well of methanol dication, CH_3OH^{2+}, upon the second ionization by the probe laser pulse, the metastable CH_3OH^{2+} thus prepared could not be decomposed into CH_3^+ and OH^+. Because of this trapping of the wave packet in the quasi bound well of CH_3OH^{2+}, a high E_{kin} component could not be seen in Figure 4.3(a).

In Figure 4.3(a), the low E_{kin} component starts appearing at $\Delta t \sim 20$ fs in the non-migration pathway. This ultrashort induction period of ~ 20 fs represents the duration of time required for the dissociative component of the wave packet to reach the internuclear distance at which the PES of CH_3OH^{2+} becomes repulsive, leading to the decomposition into $CH_3^+ + OH^+$.

4.3.3 Wave packet motion on potential energy surfaces

In the present study, ionization is achieved by a few-cycle pump laser pulse whose duration, 6.0(5) fs, is much shorter than any vibrational periods of CH_3OH. Therefore,

the geometrical structure of CH_3OH^+ generated by the pump laser pulse is estimated to be close to the geometrical structure of CH_3OH in the electronic ground state. This means that the dissociation dynamics of CH_3OH^+ prepared by the pump laser pulse may be close to that of CH_3OH^+ prepared by one-photon ionization. Therefore, a previous study of photoelectron spectroscopy of CH_3OH [10] can be referred to when the electronic states of CH_3OH^+ prepared by a few cycle pump laser pulse are discussed.

When CH_3OH^+ is prepared in the electronic ground state by the Franck-Condon projection, the dissociation into CH_3^+ ($\tilde{X}^1A_1$) and OH ($X^2\Pi$) does not proceed because CH_3OH^+ is prepared in the region below the dissociation limit located at 3.0 eV [10, 11] measured from the vibrational ground state of CH_3OH^+. When CH_3OH^+ is prepared in the vibrationally highly excited states of the first excited $\tilde{A}$ state whose vibrational energy is higher than 1.7 eV [10], the dissociation can proceed. It was argued in Refs. [12, 13] that CH_3OH^+ prepared in the second $\tilde{B}$ and/or third $\tilde{C}$ electronic states decays rapidly into the $\tilde{A}$ state via internal conversion and that the dissociation proceeds on the potential energy surface (PES) of the $\tilde{A}$ state. Therefore, it is highly probable in the present study that the wave packet is prepared in the vibrationally highly excited state of the $\tilde{A}$ state of CH_3OH^+ by a pump laser pulse.

As for the migrated species $CH_2OH_2^+$, no theoretical calculations have been reported on the shape of the PESs of the electronically excited states, to the best of our knowledge. In our previous study [5], we obtained theoretically the two dimensional PES of the electronic ground state of CH_3OH^+ as a function of the two geometrical

parameters, R (the C-O bond distance) and θ (the angle between the C-O bond axis and the line connecting the center of the C-O bond and one hydrogen atom in the methyl group). As shown in Figure 4.4, there is a saddle point on the PES covering the non-migrated (CH_3OH^+) and migrated ($CH_2OH_2^+$) geometrical configurations, which can be regarded as a transition state of the hydrogen migration reaction, separating the well bound along the C-O distance in the non-migrated geometrical configuration and the well bound along the C-O distance in the migrated configuration. If a wave packet migrating from the non-migrated configuration flows into the bound well in the electronic ground state in the migrated geometrical configuration, the motion of the wave packet in the migrated geometrical configuration may be interpreted using the PES shown in Figure 4 obtained by our quantum chemical calculation (UB3LYP/aug-cc-pVTZ) [5].

The oscillation period of the C-O stretching vibration at the equilibrium point of the migrated configuration, $CH_2OH_2^+$, is estimated to be ∼36 fs using this electronic ground state PES. Because the wave packet entering into the valley in the migrated configuration is expected to be expressed as a linear combination of vibrationally excited states in the C-O stretching mode, the oscillation period of the wave packet is expected to be considerably larger than the oscillation period of 36 fs due to the anharmonicity in the C-O stretching mode. Therefore, the observed oscillation period of ∼80 fs is consistent with the theoretical estimate.

It has been known from photoelectron spectroscopy [10] that the Franck-Condon distribution in the electronic ground state of CH_3OH^+ covers the vibrational energy ranging between 0 and 1.2 eV. In the PES obtained in Ref. [5], the height of the
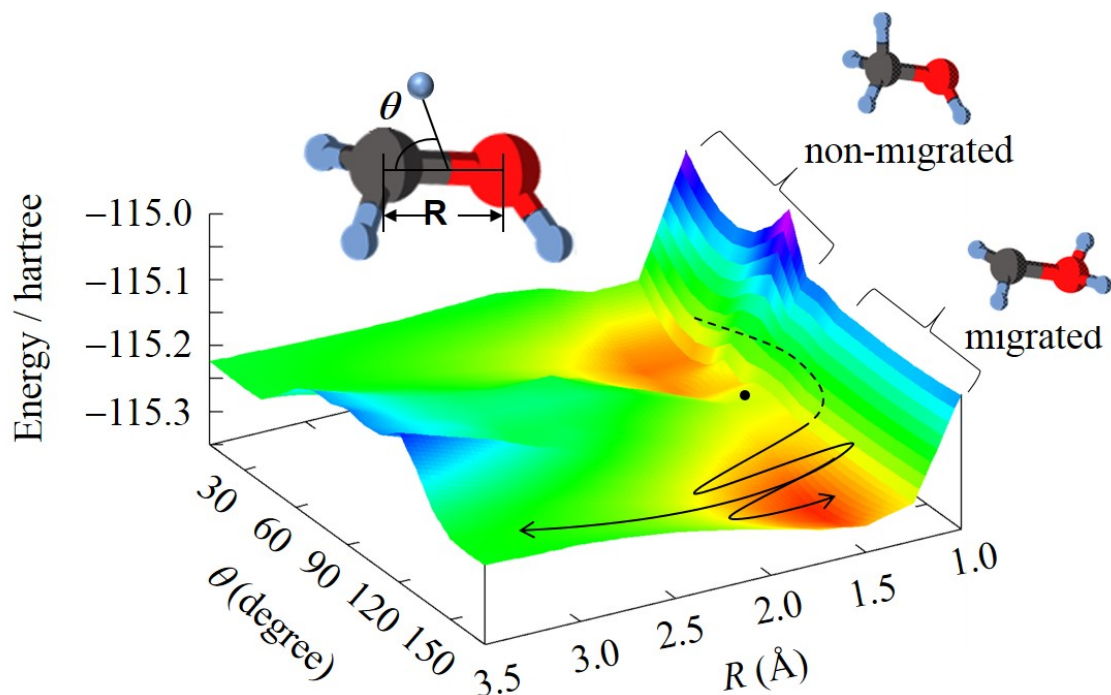
Figure 4.4: The trajectory of the wave packet migrating into the bound well of the migrated geometrical configuration of $CH_2OH_2^+$ estimated on the basis of the recorded E_{kin} distributions of the migration pathway shown in Figure 4.3(b). The dashed-line part of the trajectory line represents that the wave packet migrates from the $\tilde{B}$ or higher-lying electronically excited states in the non-migrated geometrical configuration. The two dimensional PES $V(R, \theta)$ is that of the electronic ground $\tilde{X}$ state of CH_3OH^+ calculated by Gaussian 09 (UB3LYP/aug-cc-pVTZ) obtained in Ref. [5]. All the structural parameters other than R and θ are optimized in the calculation of the PES. The definitions of R and θ are shown in the inset. The black dot represents the position of the transition state between CH_3OH^+ and $CH_2OH_2^+$.

transition state for the migration reaction on the PES of the electronic ground state measured from the bottom of the non-migrated well is 1.5 eV, and the recent theoretical calculations [14] shows that the height of the transition state falls in the range of $1.05 \sim 1.29$ eV, depending on the levels of the density functional theory calculations. These theoretical calculations [5, 14] showed that CH_3OH^+ prepared in the electronic ground state could not gain sufficient energy to go over the potential barrier for the hydrogen migration reaction. Therefore, the wave packet flowing into the potential valley of the migrated configuration is considered to be originated from the non-migrated CH_3OH^+ prepared initially in an electronically excited state.

Note that the appearance energy of CH_2^+ is 14.0 eV and the higher energy tail of the photoelectron distribution assignable to the $\tilde{A}$ state of CH_3OH^+ extends only to about 14.0 eV [10, 11], which is nearly equal to the appearance energy of CH_2^+, it is less probable that the migration starts from the $\tilde{A}$ state to form CH_2^+. Therefore, it is plausible that the excited states, from which CH2+ can eventually be generated after the migration, is higher lying electronically excited states such as the $\tilde{B}$ and $\tilde{C}$ states. It is then possible in the course of the migration that the wave packet initially prepared in the $\tilde{B}$ and/or $\tilde{C}$ states of CH_3OH^+ is transferred into the electronic ground state of migrated $CH_2OH_2^+$ via internal conversion in a similar manner to that proceeding through the conical intersection associated with the motion of the hydrogen atom in the hydroxyl group of CH_3OH [12, 13].

For more precise discussion, one needs to consider the motion of a wave packet on the PES having higher dimension. However, major dynamical motions that we have so far found experimentally are (i) the migration of one of the three hydrogen atoms

in the methyl group of CH_3OH^+ and (ii) the C-O bond breaking. Thus the interpretation based on the present two-dimensional PES reported above is expected to provide the essential aspect of the characteristic vibration and bifurcation dynamics of the wave packet occurring after the hydrogen migration.

4.4   Conclusion

We have probed ultrafast hydrogen migration in CH_3OH^+ at real time by pump-probe measurements using few-cycle near-IR laser pulses. From the resultant temporal evolution of the distributions of the released kinetic energies of the fragment ions, we have reached the following conclusions: (i) The C-O bond breaking, $CH_3OH^+ \rightarrow CH_3^+ + OH$, proceeds on the PES of the first electronically excited $\tilde{A}$ state in the non-migrated geometrical configuration (CH_3OH^+), (ii) The hydrogen migration, $CH_3OH^+ \rightarrow CH_2OH_2^+$, starts from CH_3OH^+ prepared on the PES of the $\tilde{B}$ or the higher lying electronically excited states and the nuclear wave packet is transferred through the internal conversion into the bound part of the PES of the electronic ground state in the migrated geometrical configuration in 25 fs. (iii) The wave packet flown into the migrated geometrical configuration vibrates at 1.5 cycles in the bound well and bifurcates at $\sim$150 fs into the bound component kept in the bound well to vibrate further and the dissociative component leading the C-O bond breaking, $CH_2OH_2^+ \rightarrow CH_2^+ + H_2O$. On the basis of our experimental data, we have constructed rough landscape images of the two-dimensional PES of the different electronic states on which the migrating nuclear wave packet evolves in the femtosecond time domain.

References

[1] A. Hishikawa, H. Hasegawa, and K. Yamanouchi. Hydrogen migration in acetonitrile in intense laser fields in competition with two-body Coulomb explosion. *Journal of Electron Spectroscopy and Related Phenomena*, 141:195–200, 2004.

[2] T. Okino, Y. Furukawa, P. Liu, T. Ichikawa, R. Itakura, K. Hoshina, K. Yamanouchi, and H. Nakano. Coincidence momentum imaging of ultrafast hydrogen migration in methanol and its isotopomers in intense laser fields. *Chemical physics letters*, 423:220–224, 2006.

[3] H. Xu, T. Okino, and K. Yamanouchi. Ultrafast hydrogen migration in allene in intense laser fields: Evidence of two-body Coulomb explosion. *Chemical Physics Letters*, 469:255–260, 2009.

[4] H. Xu, T. Okino, and K. Yamanouchi. Tracing ultrafast hydrogen migration in allene in intense laser fields by triple-ion coincidence momentum imaging. *The Journal of Chemical Physics*, 131, 2009.

[5] H. Xu, C. Marceau, K. Nakai, T. Okino, S. L. Chin, and K. Yamanouchi. Communication: Two stages of ultrafast hydrogen migration in methanol driven by intense laser fields. *The Journal of Chemical Physics*, 133, 2010.

[6] S. Miura, T. Ando, K. Ootaka, A. Iwasaki, H. Xu, T. Okino, K. Yamanouchi, D. Hoff, T. Rathje, G. G. Paulus, M. Kitzler, A. Baltuška, S. Giuseppe, and N. Mauro. Carrier-envelope-phase dependence of asymmetric C-D bond break-

ing in C_2D_2 in an intense few-cycle laser field. *Chemical Physics Letters*, 595-596:61 – 66, 2014.

[7] M. Nisoli, S. D. Silvestri, and O. Svelto. Generation of high energy 10 fs pulses by a new pulse compression technique. *Applied Physics Letters*, 68:2793–2795, 1996.

[8] H. Hasegawa, A. Hishikawa, and K. Yamanouchi. Coincidence imaging of Coulomb explosion of CS_2 in intense laser fields. *Chemical physics letters*, 349:57–63, 2001.

[9] J. R. Birge, R. Ell, and F. X. Kärtner. Two-dimensional spectral shearing interferometry for few-cycle pulse characterization. *Optics Letters*, 31:2063–2065, 2006.

[10] L. Karlsson, R. Jadrny, L. Mattsson, F. T. Chau, and K. Siegbahn. Vibrational and vibronic structure in the valence electron spectra of CH_3X molecules (X= F, Cl, Br, I, OH. *Physica Scripta*, 16:225, 1977.

[11] P. Warneck. Photoionisation von methanol und formaldehyd. *Zietschrift fuer Naturforshung A*, 26:2047, 1971.

[12] C. Galloy, C. Lecomte, and J. C. Lorquet. Unimolecular reaction paths of electronically excited species. III. Production of CH_3^+ ions from CH_3OH^+ as an example of isolated state dissociation. *The Journal of Chemical Physics*, 77:4522–4528, 1982.

[13] S. Borkar, B. Sztáray, and A. Bodi. Dissociative photoionization mechanism of methanol isotopologues (CH_3OH, CD_3OH, CH_3OD and CD_3OD) by iPEPICO: energetics, statistical and non-statistical kinetics and isotope effects. *Physical Chemistry Chemical Physics*, 13:13009–13020, 2011.

[14] B. Thapa and H. B. Schlegel. Molecular dynamics of methanol monocation (CH_3OH^+) in strong laser fields. *The Journal of Physical Chemistry A*, 118:1769–1776, 2014.

5 Periodical H_3^+ emission from CH_3OH^{2+} by pump-probe coincidence momentum imaging using few-cycle intense laser pulses

5.1 Introduction

When molecules are irradiated with a femtosecond laser pulse whose pulse duration is shorter than the periods of molecular vibration, a vibrational wave packet can be created within molecules, and the motion of such a wave packet has been identified by a pump-prove technique [1]. In our recent study, we investigated the ultrafast hydrogen migration in methanol cation, $CH_3OH^+ \rightarrow CH_2OH_2^+$, by the pump-probe coincidence momentum imaging method with few-cycle laser pulses [2]. The vibrational wave packet transferred into the migrated configuration was found to oscillate along the C-O bond and bifurcate into to one component keeping oscillating and the other component departing from the molecular region leading to the C-O bond breaking.

In the present study, H_3^+ emission from CH_3OH^{2+} was investigated by the few-cycle pump-probe coincidence momentum imaging method and the following three two-body Coulomb explosion pathways from doubly charged methanol were identified:

H^+ ejection Coulomb explosion pathway
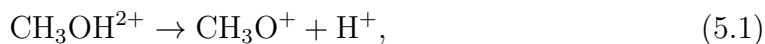
$$CH_3OH^{2+} \rightarrow CH_3O^+ + H^+, \qquad (5.1)$$

H_2^+ ejection Coulomb explosion pathway

$$CH_3OH^{2+} \to CH_2O^+ + H_2^+, \tag{5.2}$$

H_3^+ ejection Coulomb explosion pathway

$$CH_3OH^{2+} \to CHO^+ + H_3^+. \tag{5.3}$$
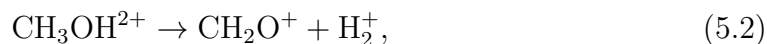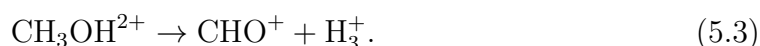
In addition to the two body Coulomb explosion pathways, the following two three-body decomposition pathways,

H^+ ejection three-body decomposition pathway

$$CH_3OH^{2+} \to CHO^+ + H^+ + H_2, \tag{5.4}$$

H_2^+ ejection three-body decomposition pathway

$$CH_3OH^{2+} \to CHO^+ + H_2^+ + H, \tag{5.5}$$
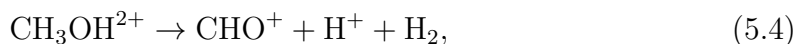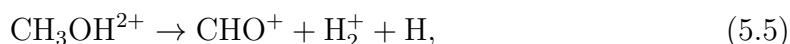
were extracted from the covariance mapping method. It was found that the ion yields of the H^+ ejection Coulomb explosion pathway (5.1) and the H_3^+ ejection Coulomb explosion pathway (5.3) periodically change and the period was found to be close to the vibrational period of C-O stretching vibration of CH_3OH^+.

Because the dissociation energies of CH_3OH^{2+} into these two pathways are known to be the lowest among all the decomposition pathways, it was considered that, when

H_3^+ and H^+ signals increase, $CH_3OH_2^+$ is prepared by the pump laser pulse in the energy region where only these two dissociation pathways are energetically allowed, while, when H_3^+ and H^+ signals decrease, it is prepared in the higher energy region so that it can be decomposed into fragments through the other energetically open pathways with larger probabilities. The oscillatory profiles of the yields of these two pathways were interpreted by the motion of a vibrational wave packet prepared on the potential energy surface (PES) of singly charged CH_3OH^+ prepared by the pump laser pulse. This mechanism of the periodical channel closing for the dissociation pathways having the higher lying threshold was supported by the two abundant three body decomposition pathway of CH_3OH^{2+}, (5.4) and (5.5), whose thresholds are located above the dissociation energies for the lowest energy pathways (1) and (3) only by ~ 1 eV and $3 \sim 4$ eV [3], respectively.

5.2 Experimental setup

The details of our experimental setup were described in the previous report [2]. Briefly, few-cycle laser pulses were generated by a hollow-core fiber compression technique using an output of a CPA femtosecond Ti:sapphire laser system (800 nm, 5 kHz, 0.6 mJ, 30 fs). The few-cycle laser pulses were introduced into a Michelson interferometer to generate pump and probe pulses. The optical time delay Δt between the pump and probe laser pulses was varied in the range between -20 fs and 500 fs using a piezo-controlled optical stage. The pulse duration was measured to be 6.0(5) fs. Both the pump and probe laser pulses were focused onto an effusive molecular beam of methanol in a vacuum chamber by a concave mirror ($f = 150$

mm). Both the laser polarization of the pump and that of the probe laser pulses were set to be parallel to the propagation axis of the molecular beam. The focal intensity was estimated to be $2.1(2) \times 10^{14} \text{W/cm}^2$.

The fragment ions generated from methanol were guided by a static electric field toward a two-dimensional position sensitive detector (HEX120, RoentDek) in the velocity map imaging configurations. From the flight time of the fragment ions and the position on the detector plane where the fragment ions hit, the momentum vectors of the fragment ions were determined. The two-body Coulomb explosion pathways of CH_3OH^{2+} were extracted by the CMI method and the released kinetic energy E_{kin} were plotted as a function of the time delay Δt.

5.3 Results and discussion

5.3.1 Extraction of pump-probe signals

Figure 5.1 shows the E_{kin} distributions of the two-body Coulomb explosion pathways, (a)-(c), and the two three-body decomposition pathways, (d) and (e), as a function of Δt. These E_{kin} distributions include the signals generated by the pump laser pulse only or probe laser pulse only because methanol dication can also be generated by a single laser pulse. The E_{kin} distributions $Y_{\text{diff}}(E_{\text{kin}}, \Delta t)$ generated from methanol dication, which is sequentially ionized by the pump and probe laser pulses, were obtained by subtracting the signals generated with the pump laser pulse $Y_{\text{pump}}(E_{\text{kin}})$ and with the probe laser pulse $Y_{\text{probe}}(E_{\text{kin}})$ from the E_{kin} distributions $Y_{\text{pump}-\text{probe}}(E_{\text{kin}}, \Delta t)$ shown in Fig. 2 as

(a) $CH_3OH^{2+} \rightarrow CH_3O^+ + H^+$

(b) $CH_3OH^{2+} \rightarrow CH_2O^+ + H_2^+$

(c) $CH_3OH^{2+} \rightarrow CHO^+ + H_3^+$

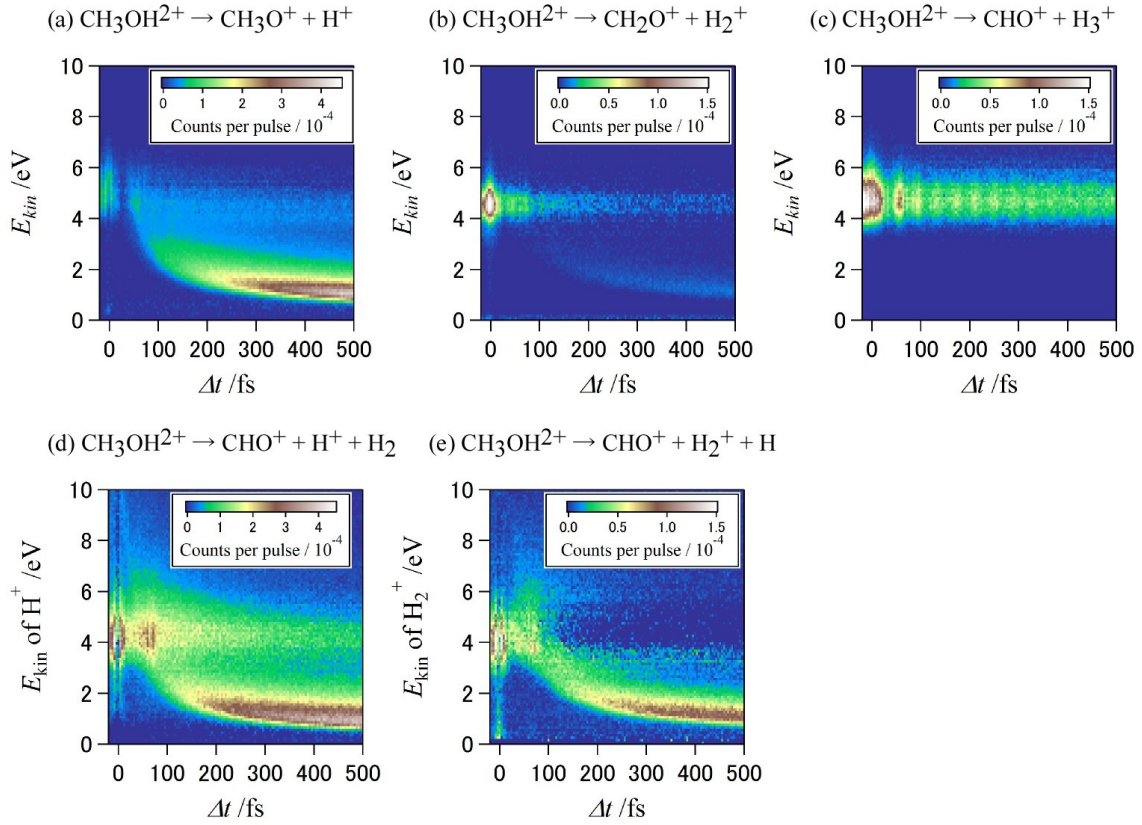(d) $CH_3OH^{2+} \rightarrow CHO^+ + H^+ + H_2$

(e) $CH_3OH^{2+} \rightarrow CHO^+ + H_2^+ + H$
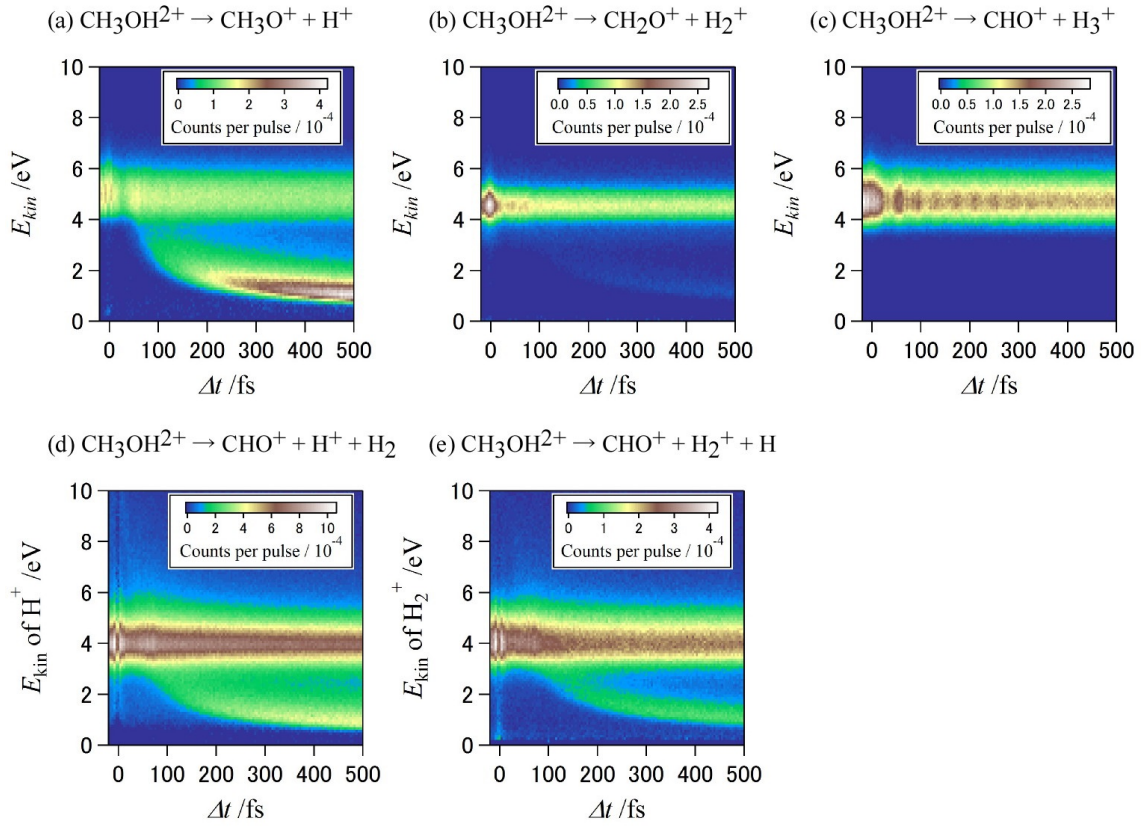
Figure 5.1: The E_{kin} distributions of the (a) H^+, (b) H_2^+ and (c) H_3^+ ejection Coulomb explosion pathways (5.1)-(5.3), (d) the E_{kin} distribution of H^+ through the H^+ ejection three-body decomposition pathway (5.4) and (d) the E_{kin} distribution of H_2^+ through the H_2^+ ejection three-body decomposition pathway (5.5) as a function of Δt.

$$Y_{\text{diff}}(E_{\text{kin}}, \Delta t) = Y_{\text{pump-probe}}(E_{\text{kin}}, \Delta t) - (Y_{\text{pump}}(E_{\text{kin}}) + \alpha Y_{\text{probe}}(E_{\text{kin}})), \qquad (5.6)$$

where α is a correction factor describing a depletion of sample molecules by irradiating the pump laser pulse. As the value of α, $\alpha = 0.79(5)$ was adopted, which was obtained in Ref. [2] by comparing the total ion yields obtained with the pump laser pulse only, the probe laser pulse only, and the pump and probe laser pulses.

5.3.2 The E_{kin} distributions of the dissociation pathways of methanol dication

Figure 5.2 shows the background-subtracted E_{kin} distributions in the three Coulomb explosion pathways, (a)-(c), and the two three-body decomposition pathways, (d) and (e), as a function of Δt. There are two types of components in these E_{kin} distributions: (i) the component whose peak energy position decreases monotonically as Δt increases and (ii) the component keeping the high E_{kin} value, 4~5 eV. The signal intensities of the high E_{kin} component decrease significantly from those in Fig. 5.1 in all the decomposition pathways because most of the signals in the high E_{kin} components are generated by single laser pulses. The lower energy component (i) in the H^+ ejection pathways, (1) and (4), and that in the H_2^+ ejection pathways, (2) and (5), reflect respectively the dynamics of the H-atom loss pathway,

H-atom loss pathway

$$CH_3OH^+ \rightarrow CH_3O^+ + H, \qquad (5.7)$$

(a) $CH_3OH^{2+} \rightarrow CH_3O^+ + H^+$

(b) $CH_3OH^{2+} \rightarrow CH_2O^+ + H_2^+$

(c) $CH_3OH^{2+} \rightarrow CHO^+ + H_3^+$

(d) $CH_3OH^{2+} \rightarrow CHO^+ + H^+ + H_2$

(e) $CH_3OH^{2+} \rightarrow CHO^+ + H_2^+ + H$
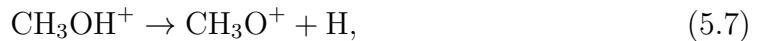
Figure 5.2: The background-subtracted E_{kin} distributions of the (a) H^+, (b) H_2^+ and (c) H_3^+ ejection Coulomb explosion pathways (5.1)-(5.3), (d) the background-subtracted E_{kin} distribution of H^+ through the H^+ ejection three-body decomposition pathway (5.4) and (d) the background-subtracted E_{kin} distribution of H_2^+ through the H_2^+ ejection three-body decomposition pathway (5.5) as a function of Δt.

and the dynamics of the H_2 loss pathway,

H_2 loss pathway

$$CH_3OH^+ \rightarrow CH_2O^+ + H_2. \tag{5.8}$$
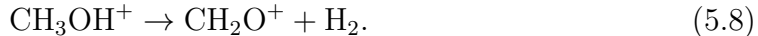
from CH_3OH^+ prepared by the pump laser pulses.

When an H-atom, departing from the CH_3O^+ moiety in the course of the dissociation (5.7), is ionized by the probe pulse, the Coulomb repulsion energy between CH_3O^+ and H^+ in (5.1) and that between CHO^+ and H^+ in (5.4) are converted into their translational energies. As the distance between the two fragments in the singly charged manifold increases during the pump-probe delay time Δt, the released kinetic energy E_{kin} decreases, which is consistent with the delay time dependence of the low kinetic energy component in Figs. 5.1 (a) and (d).

Similarly, when H_2, departing from the CH_2O^+ moiety in the course of the dissociation (5.8), is ionized by the probe pulse, the Coulomb repulsion energy between CH_2O^+ and H_2^+ in (5.2) and that between CHO^+ and H_2^+ in (5.5) are converted into their translational energies. As the distance between the two fragments in the singly charged manifold increases during the pump-probe delay time Δt, the released kinetic energy E_{kin} decreases, which is consistent with the delay time dependence of the low kinetic energy component in Figs. 5.1(b) and (e).

In the two-body Coulomb explosion pathways (5.1)-(5.3), the high E_{kin} component is commonly seen. These high energy components represent the existence of stable CH_3OH^+ prepared by the pump laser pulse. In the H_3^+ ejection Coulomb explosion pathway (5.3), the signal intensity in the high E_{kin} component periodically
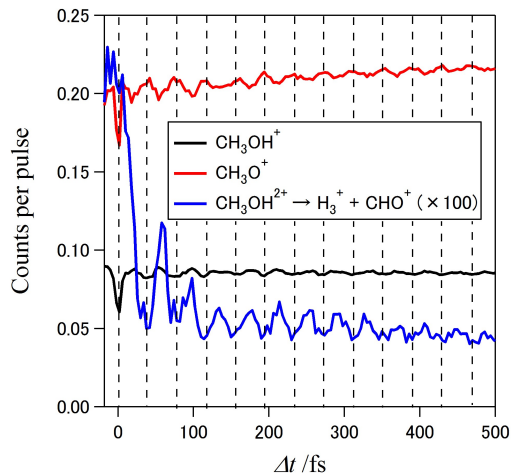
Figure 5.3: Ion yields of CH_3OH^+, CH_3O^+ and H_3^+ ejection Coulomb explosion pathway as a function of Δt.

increases with the period of $\sim$38 fs starting from $\Delta t = 58$ fs as shown in Fig. 5.2 (c), and this periodical structure continues beyond 500 fs.

It was also found that the ion yields of parent ion CH_3OH^+ and CH_3O^+ increases with the period of $\sim$38 fs as shown in Fig. 5.3. The peak position of the increase in the CH_3OH^+ yield is the same as the H_3^+ ejection Coulomb explosion pathway (5.3), that is, the oscillation in the CH_3OH^+ yield is in phase with respect to the oscillation in the H_3^+ yield, whereas the CH_3O^+ yield takes the local maxima when the intensity the H_3^+ yield takes the local maxima, that is, the oscillation in the CH_3O^+ yield is out of phase by π with respect to the oscillation in the H_3^+ yield.

5.3.3 Extraction of the ion yield oscillations

In order to extract the frequency of the ion yield oscillation, the Fourier transformation was performed on the ion yields of H_3^+ (pathway (5.3)), CH_3O^+ (pathway (5.7)), and CH_3OH^+ in the range of $120 < \Delta t < 500$ fs after subtracting a contin-

73
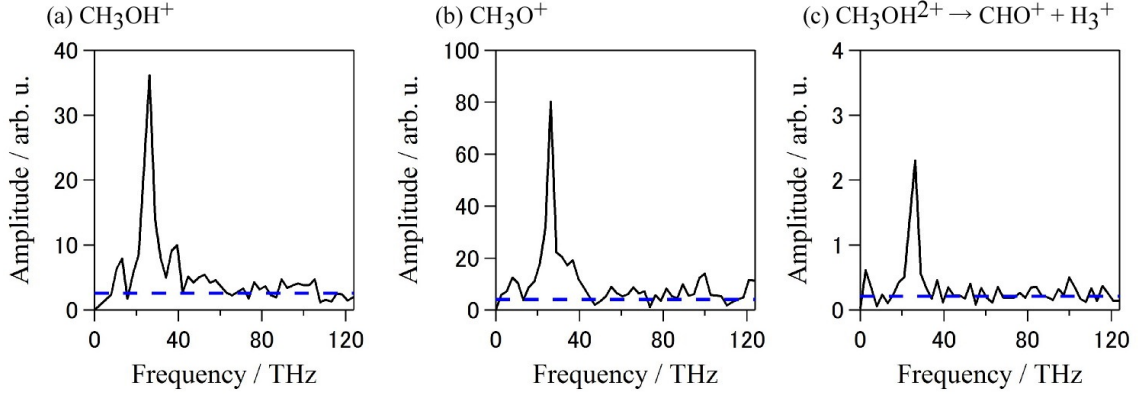
Figure 5.4: The Fourier-transformed ion yields of (a) CH_3OH^+, (b) CH_3O^+ and (c) H_3^+ in the range of $120 < \Delta t < 500$ fs after subtracting a continuum component fitted with an exponential curve. The blue broken curves show the standard deviation calculated from the number of the signals in each pathway.

uum component fitted with an exponential curve. As shown in Fig. 5.4, in all the three Fourier transformed (FT) spectra, a peak at ~ 26 THz, corresponding to the period of ~ 38 fs, is commonly identified.

In Figs. 5.5 (a) and (b), the ion yields of the pathways (5.11) and (5.2) are shown as a function of Δt. The signal intensity becomes maximum at $\Delta t \sim 0$ fs because the pump and probe laser pulses constructively interferes and the ionization probability increases. After the short time zone in the range below $\Delta t \sim 10$ fs, where the pump and probe pulses interfere constructively and destructively, the signal intensities increase in the range of $20 < \Delta t < 80$ fs, and gradually decrease after 80 fs. The Fourier transformation was also performed on the ion yields of H^+ (pathway (5.1)) and H_2^+ (pathway (5.2)) in their high E_{kin} components in the range of $120 < \Delta t < 500$ fs after subtracting a continuum component fitted with an exponential curve and the results are shown in Figs. 5.5 (c) and (d).

In the FT spectrum of the ion yield of the H^+ ejection pathway (5.1) (Fig.

74
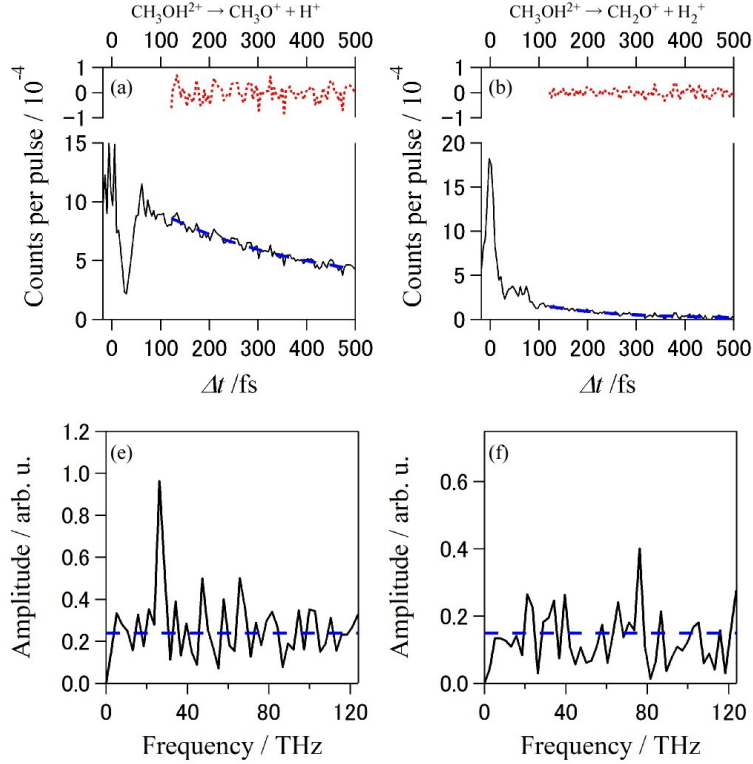
Figure 5.5: Ion yields of H^+ ejection Coulomb explosion pathway ((a) and (c)) and H_2^+ ejection Coulomb explosion pathway ((b) and (d)) in the their high E_{kin} components ($E_{kin} > 3.5$ eV). The Δt dependence of the ion yields are shown in (a) and (b) with black curves. Blue broken curves: fitted ion yields with exponential curve from 120 fs to 500 fs. Red dotted curves: residual ion yields after the subtraction of the fitted ion yields. FT spectra of the residual ion yields in each pathway are shown in (c) and (d) with black curves. Blue broken curves: standard deviation calculated from the number of the signals in each pathway.

5.5(c)), a peak can be identified at $\sim$26 THz, which is consistent with the frequency identified in the ion yield of H_3^+ ejection pathway, while no significant peaks can be found in the FT spectrum for the H_2^+ ejection pathway in the entire range of the frequency (Fig. 5.5(d)). The peak positions of the background subtracted ion yield of H^+ are 134, 174, 210,... fs as shown in the red dotted curve in Fig. 5.5 (a). This oscillation of the ion yield of H^+ is found to be in phase with the H_3^+ ejection pathway.

5.3.4 Origin of the ion yield oscillations

It is possible that the periodical changes in the ion yields identified above reflect the motion of the vibrational wave packet of CH_3OH^+ created by the pump laser pulse. Considering that a few cycle laser pulse is employed to create CH_3OH^+, its geometrical structure could not be varied so much during the pulse duration of $\sim$6 fs. Therefore, the vibrational wave packet is prepared in the Franck-Condon region, that is, it is prepared on a potential energy surface of CH_3OH^+ at the geometrical structure close to the equilibrium geometrical structure of CH_3OH in the electronic ground state.

In the photoelectron spectrum of CH_3OH [4], the energy spacing of $\sim$111 meV identified in the series of peaks in the spectrum was assigned to the C-O stretching vibrational progression of the electronic ground state of CH_3OH^+, and, from this energy spacing, the vibrational wavenumber of the C-O stretching was estimated to be 894 cm^{-1}, which corresponds to the frequency of 26.8 THz. Because the frequency of the oscillations in the ion yields identified in the present study, $\sim$26

THz, is in good agreement with this C-O stretching frequency, it is highly possible that the oscillations reflect the C-O stretching motion of the vibrational wave packet prepared in the electronic ground state of CH_3OH^+.

From the quantum chemical calculations, the equilibrium C-O internuclear distance of CH_3OH, CH_3OH^+ and CH_3OH^{2+} were obtained 1.42, 1.37 and 1.19 Å, respectively [5, 6], indicating that the vibrational wave packet of CH_3OH^+ prepared by the pump laser pulse is expected to start moving toward the equilibrium structure, that is, the C-O bond distance starts shrinking immediately after the preparation of CH_3OH^+.

After the vibrational wave packet reaches the shortest C-O bond distance at a half of the vibrational period, ∼19 fs, it starts to move back to the longer C-O distance region until it reaches the original position where it was prepared by the pump pulse. This vibrational motion with the period of ∼38 fs is expected to repeat. The H_3^+ ejection pathway has the minimum ion yields at 38, 78, 114,... fs, which are close to the multiples of the period, and the maxima at 58, 98, 134,... fs, which are close to the multiples of the period plus a half of the period. This means that the ion yield of H_3^+ increases every time the probe laser pulse is introduced at the moment when the oscillating C-O bond distance becomes the shortest.

Because the theoretical estimate of the equilibrium C-O internuclear distance of CH_3OH^{2+} is shorter than that of CH_3OH^+ by 0.18 Å [6], the wave packet prepared in CH_3OH^{2+} by the ionization by the pump laser from CH_3OH^+ is expected to have lower energy when the C-O bond distance becomes shorter. Therefore, it is probable from the discussion above that the ion yield of H_3^+ increases when the internal energy

of CH_3OH^{2+} is lower. For the H^+ ejection, the same argument should hold because the oscillation of the the H^+ ion yield in the H^+ ejection Coulomb explosion pathway is in phase with the H_3^+ ejection, that is, the ion yield of H^+ increases when the internal energy of CH_3OH^{2+} is lower.

It has been know that the H^+ and H_3^+ ejection Coulomb explosion pathways have the lowest threshold energy among all the decomposition pathways of CH_3OH^{2+} [3]. The next lowest decomposition pathway is the H^+ ejection pathway (5.4), which has the threshold energy higher by ~ 1 eV than the pathway (5.1) and (5.3). This means that as long as CH_3OH^{2+} is produced in the energy threshold of the pathway (5.4), it can only be decomposed through the pathways (5.1) and (5.3).

On the other hand, when CH_3OH^{2+} is prepared in the energy region above the threshold energy for the pathway (5.4), it can be decomposed into fragments not only through the pathway (5.1) and (5.3), but also through the pathway (5.4). Judging from the numbers of events,the H^+ ejection pathway (5.4) has the largest ion yield among all the decomposition pathways (5.1)-(5.5); the ion yield of the high E_{kin} component of the H^+ ejection pathway (5.4) is around 3 times higher than those of the pathways (5.1) and (5.3) at $\Delta t \sim 500$ fs. Furthermore, no oscillations were found in the ion yield of the pathway (5.4). Therefore, the opening of the pathway (5.4) may suppress the decomposition through the pathways (5.1) and (5.3), resulting in the decrease in the yields of H^+ and H_3^+.

The ion yield oscillation of the CH_3OH^+ is in phase with the H_3^+ ejection Coulomb explosion pathway (5.4) and the oscillation of CH_3O^+ is out of phase. Because these oscillation amplitudes have the same order of magnitude, the yield oscillations are

ascribed to the H-atom loss decomposition pathway (5.7) through which the ion yield of CH_3OH^+ decreases while the ion yield of CH_3O^+ increases.

According to the photoelectron spectroscopy and the photoelectron-photoion coincidence study [4, 7], the CH_3O^+ has the lowest appearance energy, which is 0.6 eV above the adiabatic ionization energy of CH_3OH^+, showing that the dissociation pathway (5.7) has the lowest threshold energy for the dissociation among all the decomposition processes of CH_3OH^+. If CH_3OH^+ is prepared on the electronic ground state by the pump laser pulse, it can be resonantly excited to the first electronically excited $\tilde{A}$ state by the probe laser pulse whose photon energy is in the range between 1.3 and 1.9 eV because the energy difference between the vertical ionization energy to the $\tilde{A}$ state and that to the electronic ground state is ~ 1.7 eV, which is in the range of the one photon energy. Once CH_3OH^+ is excited to the $\tilde{A}$ state, its energy exceeds the threshold energies for the other decomposition pathways such as the H-atom loss pathway (5.7) and the H_2 loss pathway (5.8).

Therefore, the periodical increase in the ion yield of CH_3O^+ and the periodical decrease in the ion yield of CH_3OH^+ at Δt being the multiples of the period of ~ 38 fs can be ascribed to the resonance excitation of CH_3OH^+ in the electronic ground state to the $\tilde{A}$ state by the pump laser pulse, achieved when the wave packet oscillating along the C-O bond comes back to the original distance.

5.4　Conclusion

The pump-probe measurements of CH_3OH was performed with few-cycle pulses. It was revealed that the ion yields of the H^+ and H_3^+ ejection Coulomb explosion

pathways oscillate in phase with the period of $\sim$26 THz, which was interpreted by the wave packet oscillation along the C-O bond in CH_3OH^+ prepared by the pump laser pulse and the associated variation of the internal energy of CH_3OH^{2+} gained by the probe laser pulse. When the C-O distance is at the inner turning point of the C-O stretching vibration in CH_3OH^+, the ionization achieved by the probe laser pulse prepares CH_3OH^{2+} in the low energy region, where only H^+ and H_3^+ can be generated through the Coulomb explosion, while, when the C-O distance becomes larger, the ionization prepares CH_3OH^{2+} can decompose into fragments through other pathways with the larger yields, which suppresses the decomposition into H^+ and H_3^+. The yield oscillation at $\sim$26 THz was also identified for CH_3OH^+ and CH_3O^+, which was interpreted by the resonant excitation of CH_3OH^+ from the electronic ground state to the first electronically excited $\tilde{A}$ state at the outer turning point of the C-O bond stretching vibration, leading to the periodical formation of CH_3O^+ from CH_3OH^+.

Appendix: Covariance mappong method and coincidence momentum imaging method

The covariance $C(N_A(\overrightarrow{p}_A), N_B(\overrightarrow{p}_B))$ of two ions, A having the momentum vector $\overrightarrow{p}_A$ and B having the momentum vector $\overrightarrow{p}_B$, is represented by the formula [8],

$$
\begin{aligned}
C(N_A(\overrightarrow{p}_A), N_B(\overrightarrow{p}_B)) &= \langle (N_A(\overrightarrow{p}_A) - \langle N_A(\overrightarrow{p}_A)\rangle)(N_B(\overrightarrow{p}_B) - \langle N_B(\overrightarrow{p}_B)\rangle)\rangle \\
&= \langle N_A(\overrightarrow{p}_A)N_B(\overrightarrow{p}_B)\rangle - \langle N_A(\overrightarrow{p}_A)\rangle\langle N_B(\overrightarrow{p}_B)\rangle, \quad (5.9)
\end{aligned}
$$

where $\langle N_{A,B}(\overrightarrow{p}_{A,B}) \rangle$, $\langle N_A(\overrightarrow{p}_A)N_B(\overrightarrow{p}_B) \rangle$, $\langle N_A(\overrightarrow{p}_A) \rangle \langle N_A(\overrightarrow{p}_A) \rangle$ are defined as

$$\langle N_{A,B}(\overrightarrow{p}_{A,B}) \rangle = \frac{1}{M} \sum_{i=0}^{M} \delta_{\overrightarrow{p}_{A,B}, \overrightarrow{p}_{A,B}^{(i)}} \tag{5.10}$$

$$\langle N_A(\overrightarrow{p}_A)N_B(\overrightarrow{p}_B) \rangle = \frac{1}{M} \sum_{i=0}^{M} \delta_{\overrightarrow{p}_A, \overrightarrow{p}_A^{(i)}} \delta_{\overrightarrow{p}_B, \overrightarrow{p}_B^{(i)}} \tag{5.11}$$

$$\langle N_A(\overrightarrow{p}_A) \rangle \langle N_A(\overrightarrow{p}_A) \rangle = \frac{1}{M^2} \sum_{i,j=0}^{M} \delta_{\overrightarrow{p}_A, \overrightarrow{p}_A^{(i)}} \delta_{\overrightarrow{p}_B, \overrightarrow{p}_B^{(j)}} \tag{5.12}$$

where $\overrightarrow{p}_{A,B}^{(i)}$ represents the momentum vector of the fragment ion obtained at the i-th laser shot, and M represents the number of laser shots. The first term in Eq. (5.9) represents the coincidence events and the second term represents the probability of detecting both A and B accidentally. The covariance of H^+ and CHO^+ was regarded as that of the H^+ ejection pathway (5.4) and the covariance of H_2^+ and CHO^+ was regarded as that of the H_2^+ ejection pathway (5.5).

In the CMI method, the contribution from accidental false coincidence events was also subtracted in a similar manner as in the covariance mapping method. The distribution of events in the six dimensional momentum space $S_{CMI}(N_A(\overrightarrow{p}_A), N_B(\overrightarrow{p}_B))$ extracted from CMI measurements can be described using the first term in Eq. (5.9), $\langle N_A(\overrightarrow{p}_A)N_B(\overrightarrow{p}_B) \rangle$, as

$$S_{CMI}(N_A(\overrightarrow{p}_A), N_B(\overrightarrow{p}_B)) = \sum_{i=0}^{M} w(\overrightarrow{p}_A^{(i)} + \overrightarrow{p}_B^{(i)})$$

$$= \iint \langle N_A(\overrightarrow{p}_A)N_B(\overrightarrow{p}_B) \rangle w(\overrightarrow{p}_A + \overrightarrow{p}_B) d\overrightarrow{p}_A d\overrightarrow{p}_B \tag{5.13}$$

where the function w represents the momentum matching condition as

$$
w = \begin{cases} 1 & \text{if } |p_{x,y}| < 4.5 \times 10^3 \text{ u m/s and } |p_{x,y}| < 2 \times 10^4 \text{ u m/s} \\ \\ 0 & \text{otherwise} \end{cases} . \qquad (5.14)
$$

and p_x, p_y and p_z represent respectively the momentum of the ion along the laser propagation direction, the direction from the crossing point of the laser and molecular beams to the detector and the propagation direction of the effusive molecular beam. The tolerance width of the function w along the z direction was set to be larger than the widths for the other two directions considering the larger momentum distribution width along the z direction than in the other two directions. The standard deviations σ_x, σ_y, and σ_z of the sum of the momenta of the fragment ions are $2.1 \times 10^3, 2.2 \times 10^3$ and 9.9×10^3 u m/s, respectively.

The distribution of false coincidence events in the six dimensional momentum space, $F(N_{\mathrm{A}}(\vec{p}_{\mathrm{A}}), N_{\mathrm{B}}(\vec{p}_{\mathrm{B}}))$, can be evaluated using the second term in Eq. (5.9) as

$$
\begin{aligned}
F(N_{\mathrm{A}}(\vec{p}_{\mathrm{A}}), N_{\mathrm{B}}(\vec{p}_{\mathrm{B}})) &= \iint \langle N_{\mathrm{A}}(\vec{p}_{\mathrm{A}}) \rangle \langle N_{\mathrm{B}}(\vec{p}_{\mathrm{B}}) \rangle w(\vec{p}_{\mathrm{A}} + \vec{p}_{\mathrm{B}}) d\vec{p}_{\mathrm{A}} d\vec{p}_{\mathrm{B}} \\
&= \frac{1}{M} \sum_{i,j=0}^{M} w(\vec{p}_{\mathrm{A}}^{(i)} + \vec{p}_{\mathrm{B}}^{(j)}) \qquad (5.15)
\end{aligned}
$$

This means the number of false coincidence events can be estimated by imposing the momentum matching conditions on the fragment ions generated by different laser shots. In order to estimate the number of false coincidence events from the

data obtained by laser pulses having similar laser parameters, the number of the false coincidence events can be estimated by applying the momentum matching conditions to the fragment ions generated by a laser pulse and those generated by the next laser pulse in the high-repetition laser pulses represented as

$$F'(N_\mathrm{A}(\overrightarrow{p}_\mathrm{A}), N_\mathrm{B}(\overrightarrow{p}_\mathrm{B})) = \sum_{i=0}^{M} w(\overrightarrow{p}_\mathrm{A}^{(i)} + \overrightarrow{p}_\mathrm{B}^{(i+1)}) \qquad (5.16)$$

References

[1] A. H. Zewail. Femtochemistry. *The Journal of Physical Chemistry*, 97:12427–12446, 1993.

[2] T. Ando, A. Shimamoto, S. Miura, K. Nakai, H. Xu, A. Iwasaki, and K. Yamanouchi. Wave packet bifurcation in ultrafast hydrogen migration in CH_3OH^+ by pump-probe coincidence momentum imaging with few-cycle laser pulses. *Chemical Physics Letters*, in press, 2015.

[3] J. H. D. Eland and B. J. Treves-Brown. The fragmentation of doubly charged methanol. *International Journal of Mass Spectrometry and Ion Processes*, 113:167–176, 1992.

[4] L. Karlsson, R. Jadrny, L. Mattsson, F. T. Chau, and K. Siegbahn. Vibrational and vibronic structure in the valence electron spectra of CH_3X molecules (X= F, Cl, Br, I, OH. *Physica Scripta*, 16:225, 1977.

[5] H. Xu, C. Marceau, K. Nakai, T. Okino, S. L. Chin, and K. Yamanouchi. Communication: Two stages of ultrafast hydrogen migration in methanol driven by intense laser fields. *The Journal of Chemical Physics*, 133, 2010.

[6] B. Thapa and H. B. Schlegel. Molecular dynamics of methanol monocation (CH_3OH^+) in strong laser fields. *The Journal of Physical Chemistry A*, 118:1769–1776, 2014.

[7] S. Borkar, B. Sztáray, and A. Bodi. Dissociative photoionization mechanism of methanol isotopologues (CH_3OH, CD_3OH, CH_3OD and CD_3OD) by iPEPICO:

energetics, statistical and non-statistical kinetics and isotope effects. *Physical Chemistry Chemical Physics*, 13:13009–13020, 2011.

[8] L. J. Frasinski, K. Codling, and P. A. Hatherly. Covariance mapping: a correlation method applied to multiphoton multiple ionization. *Science*, 246:1029–1031, 1989.

6 Summary and future perspective

In this study, I found that the ultrafast hydrogen migration in methanol take place after passing through the few-cycle laser pulses although the migration ratio is poor compared with the ultrafast hydrogen migration within the laser field, whose pulse duration is tens of femtosecond [1]. The vibrational wave packet resulting in hydrogen migration is prepared by ionizing the molecule with intense laser field. In the discussion, I assumed that the wave packet keeps initial geometrical structure of neutral methanol during the preparing process and I concluded that the C-O breaking should take place in the electronically excited states. This assumption, called Frank-Condon approximation, has been applied for one photon ionization. To confirm which electronically excited states hydrogen migration starts from, the wave packet should be prepared by one photon ionization process and observe photoelectron spectra. For that experiment, high-order harmonics of the intense laser pulses are desirable pump pulses. The one photon energy can reach to the ionization energy of hydrocarbon molecules and the time delay can be controlled easily if the driving pulse of high order harmonics are used for the probe pulse.

The CH_3^+ emission pathway from CH_3OH^+ had been investigated experimentally and theoretically [2, 3]. The theoretical study proposed that the CH_3OH^+ on the second electronically excited states through a conical intersection and the C-O bond stretches on the first excited state [3]. The strength of nonadiabatic matrix elements was calculated under the C_s symmetry and the local maximum of nonadiabatic matrix elements was found at $\angle COH=69.8°$ but the conical intersection was not shown.

At the conical intersection, the molecular structure has higher symmetry than the neighboring structure. The conical intersection has C_{2v} symmetry, $CH_2OH_2^+$ geometrical structure, if the conical intersection appears under the C_s symmetry and $\angle COH=69.8°$. It is considered that the conical intersection strongly related to the ultrafast hydrogen migration. Besides, the ultrafast H/D atom exchange process, which was observed in CD_3OH in ref. [1], is also related with the conical intersection because the conical intersection is on the trajectory of the H/D atom exchange process. It is expected that the CHD_2^+ emission from CD_3OH^+ can be observed by pump-probe experiment of CD_3OH molecule.

The electronic states contributing to the ultrafast hydrogen migration enable us to design the laser field to promote the hydrogen migration. In diatomic molecules, the vibrational wave packet is manipulated by the intense laser field thanks to the rich knowledge of the potential energy surfaces [4].

I also found that the yield of some of fragment ions periodically changes respect to the time delay. Especially, it is interesting that ion yield of the H_3^+ emission Coulomb explosion pathway, which is slow decomposition pathway, also oscillates. The origin of oscillation is assigned to the C-O stretching vibration of methanol cation. It is considered that the internal energy in methanol dication can be changed by the structure of methanol cation just before the ionization. The fragmentation ratio of methanol dication depends on the internal energy. As a result, the ion yield of the H_3^+ emission pathway, which has lowest appearance energy in all the fragmentation pathway of methanol dication, oscillates in time delay.

The assignment of periodical ion yield is based on the vibrational frequency of

methanol cation determined from the photoelectron spectra of methanol [5]. The discrepancy between the observed frequency of ion yield and the C-O stretching mode may due to the low resolution of photoelectron spectra. The C-O stretching vibration mode is coupled with torsional vibration and the torsional vibration mode can not be resolved in photoelectron spectra. In the recent experiment with zero-kinetic energy photoelectron spectroscopy [6], the vibrational energy of C-O stretching mode in CD_3OD is 710 ± 4 cm^{-1}, which is lower than previous data 763 ± 30 cm^{-1} from the photoelectron spectroscopy [7].

If the pump-probe experiment is performed in deuterated methanol, the vibrational mode can be assigned certainly because the vibrational energy levels of CD_3OD^+ are well known. Besides, partially deuterated methanol CD_3OH helps to know which geometrical structure, CDO^+ and COH^+, is formed after the emission. The theoretical study suggests that there are two geometrical structures after the H_3^+ emission. In other molecules, it is expected to observe the periodical ion yield and it helps to know the sequential excitation process of the molecules in the intense laser field.

References

[1] T. Okino, Y. Furukawa, P. Liu, T. Ichikawa, R. Itakura, K. Hoshina, K. Yamanouchi, and H. Nakano. Coincidence momentum imaging of ultrafast hydrogen migration in methanol and its isotopomers in intense laser fields. *Chemical physics letters*, 423:220–224, 2006.

[2] S. Borkar, B. Sztáray, and A. Bodi. Dissociative photoionization mechanism of methanol isotopologues (CH_3OH, CD_3OH, CH_3OD and CD_3OD) by iPEPICO: energetics, statistical and non-statistical kinetics and isotope effects. *Physical Chemistry Chemical Physics*, 13:13009–13020, 2011.

[3] C. Galloy, C. Lecomte, and J. C. Lorquet. Unimolecular reaction paths of electronically excited species. III. Production of CH_3^+ ions from CH_3OH^+ as an example of isolated state dissociation. *The Journal of Chemical Physics*, 77:4522–4528, 1982.

[4] B. Sheehy, B. Walker, and L. F. DiMauro. Phase control in the two-color photodissociation of hd$^+$. *Physical Review Letters*, 74:4799–4802, 1995.

[5] L. Karlsson, R. Jadrny, L. Mattsson, F. T. Chau, and K. Siegbahn. Vibrational and vibronic structure in the valence electron spectra of CH_3X molecules (X= F, Cl, Br, I, OH. *Physica Scripta*, 16:225, 1977.

[6] Z. Dai, S. Gao, J. Wang, and Y. Mo. Torsional energy levels of $CH_3OH^+/CH_3OD^+/CD_3OD^+$ studied by zero-kinetic energy photoelectron spec-

troscopy and theoretical calculations. *The Journal of Chemical Physics*, 141:144306, 2014.

[7] K. A. G. MacNeil and R. N. Dixon. High-resolution photoelectron spectroscopy of methanol and its deuterated derivatives: Internal rotation in the ground ionic state. *Journal of Electron Spectroscopy and Related Phenomena*, 11:315–331, 1977.

List of Figures

Acknowledgements

First of all, I would like to thank my supervisor, Prof. Kaoru Yamanouchi. He gave me a lot of valuable advice, and encouraged me throughout the thesis study. I am truly grateful to him for giving me an ideal research environment. I am also indebted to Dr. Atsushi Iwasaki for his valuable guidance in the experiments. Besides, I would like to thank Dr. Katsunori Nakai, who calculates the potential energy surface of methanol cation in this thesis. I am also grateful to other staff members in Prof. Yamanouchi's group, Prof. Tsuyoshi Kato, Prof. Huailiang Xu, Dr. Reika Kanya, Dr. Takahiro Sato and Dr. Akinori Sugiyama.

More gratitude also goes out to our experimental team, Dr. Shun Miura, Mr. Kazuki Ootaka, Mr. Akihiro Shimamoto, Ms. Mikoto Toyama and Mr. Yuki Kobayashi and to all the members of Prof. Yamanouchi's group. Last but not least, I am grateful to my family members and to my friends for their warm support.